Reassessing *CP* violation in the complex 2HDM with machine learning

Rafael Boto,[1,*] Karim Elyaouti,[1,†] Duarte Fontes,[1,‡] Maria Gonçalves,[1,2,§] Margarete Mühlleitner,[1,∥] Jorge C. Romão,[3,¶] Rui Santos,[2,4,**] and João P. Silva[3,††]

[1]*Institute for Theoretical Physics, Karlsruhe Institute of Technology, 76128 Karlsruhe, Germany*
[2]*Centro de Física Teórica e Computacional, Faculdade de Ciências, Universidade de Lisboa, Campo Grande, Edifício C8, 1749-016 Lisboa, Portugal*
[3]*Departamento de Física and CFTP, Instituto Superior Técnico, Universidade de Lisboa, Avenida Rovisco Pais 1, 1049-001 Lisboa, Portugal*
[4]*Departamento de Física, Faculdade de Ciências, Universidade de Lisboa, 1749-016 Lisboa, Portugal*

(Received 21 May 2026; accepted 13 August 2026; published 8 September 2026)

We provide a study of the parameter space of the complex 2-Higgs doublet model (C2HDM), focusing on signs of large *CP*-violating couplings of the 125 GeV Higgs boson with the fermions. The study is performed utilizing machine learning (ML) techniques developed recently for parameter space exploration, including an evolutionary strategy algorithm and novelty reward. We give particular attention to the electron electric dipole moment (eEDM). We confirm that the recently found kite diagrams are crucial for the outcome of the analysis. Moreover, their use also mitigates the dependence of the results on the scale and scheme choice of the masses in the loop diagrams. We furthermore point out that, already at the current level of experimental precision, the Barr-Zee diagrams with charm quark loops must be taken into account. The combined use of kite diagrams and ML techniques allows for the resurrection of large fermion *CP*-odd couplings for type II and flipped C2HDM when the 125 GeV Higgs coincides with the second lightest neutral scalar. This arises due to cancellations, typically of the per-mil order, which, moreover, will still be possible for a foreseeable eEDM precision down to 10^{-33} e. cm. For these cases, the constraints on the *CP*-odd couplings arises from the precision LHC measurements.

DOI: 10.1103/1pdt-tmcb

I. INTRODUCTION

T.D. Lee showed that a 2-Higgs doublet model (2HDM) allows for spontaneous *CP* violation in the scalar sector [1]. Experiments in *B*-physics [2,3] guarantee that the *CP* violation in *W* boson interactions, predicted in the Standard Model (SM), must be large. This spurred interest in a more general *CP*-violating framework in the 2HDM. In order to avoid flavor-changing neutral scalar interactions, a $\mathbb{Z}_2$ symmetry is usually employed [4,5]. This leads to a *CP*-conserving scalar sector in the 2HDM and, moreover, precludes a decoupling limit. Both problems may be solved by introducing in the potential a complex soft-symmetry breaking term (m_{12}^2). This leads to the complex 2HDM (C2HDM), which has been extensively explored in the literature; see, for example, Refs. [6–42].

Models with *CP* violation in the scalar sector must contend with potentially large contributions to the electron electric dipole moment (eEDM). The leading contributions arise from two-loop Barr-Zee diagrams [43] and extensions [44–46]. In Ref. [36] it was shown that a new class of two-loop diagrams (dubbed "kite diagrams") is essential for the gauge independence of the final result. In a subsequent article, relevant one-loop diagrams were also identified [47].

The inclusion of all relevant diagrams in the computation of the eEDM is crucial for the following two reasons. On the one hand, current experiments are extremely accurate: the 90% confidence-level limit on the eEDM reported by the ACME collaboration is 1.1×10^{-29} e.cm [48–50], while JILA quotes 4.1×10^{-30} e.cm [50]. On the other hand, in the Feynman gauge, each individual diagram can typically yield values of order 10^{-27} e.cm. Thus, in order to get substantial large *CP* violation (e.g. in

*Contact author: rafael.boto@kit.edu
†Contact author: karim.elyaouti@partner.kit.edu
‡Contact author: duarte.fontes@kit.edu
§Contact author: magoncalves@fc.ul.pt
∥Contact author: margarete.muehlleitner@kit.edu
¶Contact author: jorge.romao@tecnico.ulisboa.pt
**Contact author: rasantos@fc.ul.pt
††Contact author: jpsilva@cftp.ist.utl.pt

Higgs-fermion vertices), there needs to be a substantial cancellation among different eEDM diagrams, often of one part per mil. This forces the consideration of previously overlooked diagrams; for example, we will show that, given the current eEDM constraints, Barr-Zee diagrams involving virtual charm quarks need to be included. The expected sensitivity of future eEDM experiments has been discussed to be $\mathcal{O}(10^{-33})$ e.cm [51–53], increasing the difficulty of obtaining the necessary cancellations in a scenario of nondiscovery. Using the diagrams included in our study, we show that the cancellations can still be met for different cases of C2HDM.

The impact of eEDM measurements on the C2HDM parameter space has been considered by a number of authors [22–29]. In Ref. [29], a subset of the authors of this work revisited the C2HDM taking into account the most recent experimental results in order to quantify the amount of CP-violation that was still possible in the coupling of the SM-like Higgs to the fermions. In the C2HDM, there are three neutral scalars with mixed CP nature, denoted by h_1, h_2, and h_3, ordered by increasing masses. The Higgs particle found at Large Hadron Collider (LHC) with mass of 125 GeV [54,55] is denoted by h_{125}. All three possibilities—$h_1 = h_{125}$, $h_2 = h_{125}$ and $h_3 = h_{125}$—have been considered. The CP-even (CP-odd) $h_{125}ff$ couplings are denoted by c^e_f (c^o_f), where f denotes a fermion. The analysis is performed for each of the four $\mathbb{Z}_2$-symmetric C2HDM submodels, namely, type I, type II, lepton-specific (LS) and flipped. In Ref. [29], the particular case of the type II model with the configuration $h_2 = h_{125}$ received special attention, for reasons detailed below. For reference, we display in Table I the results found in [29] on the possibility of a large CP-odd coupling admixture to the h_{125} Yukawa couplings. In this work, we revisit this table in light of the new scanning techniques.

Valid points in the C2HDM parameter space were found in Refs. [25,29] by manually scanning close to the CP-conserving limit and iteratively enlarging the pseudoscalar component. This method was also followed for the $\mathbb{Z}_2 \times \mathbb{Z}_2$ in Ref. [57]. Using a machine-learning (ML) algorithm with an evolutionary strategy and novelty reward mechanism, it was shown in Ref. [58] that this method seriously misses valid regions of the model's parameter space and the resulting physical implications. This motivated us to revisit the C2HDM with the same ML strategy. In particular, we found that the possibility of large CP-odd Higgs-fermion couplings for the flipped type with $h_2 = h_{125}$, which seemed impossible using the usual search techniques, is revived.

ML has become an essential tool in particle physics, driven by the increasing complexity and volume of data from experiments like those at the LHC. Recent reviews [59–61] include the developments in different fronts of artificial intelligence in high-energy physics. We are interested in the validation of a beyond-the-SM (BSM) theory through constraints on its parameter space. Successful approaches to sampling the parameter space of BSMs have been developed in cases where training datasets are available [62–68]. Given the goal set on finding physical implications that we do not yet know about in highly constrained scans, we turn to search methods that do not rely on an initial set of sampled data. We consider an evolutionary strategy algorithm, first introduced in Ref. [69] to find valid and verifiable points of the model, combined with an anomaly detection used for novelty reward developed in Ref. [70], to ensure good exploration of parameter spaces and of the physical observables of the model.

TABLE I. Results for the possibility of large Yukawa couplings from Ref. [29]. A cross means that it is not possible to have large CP-odd couplings, i.e. $|c^o| \gtrsim |c^e|$. The notation τ means that c^o/c^e is limited by the direct searches for CP-violating angular correlations of tau leptons in $h_{125} \to \tau\bar{\tau}$ decays [56]. Underlined crosses indicate a change from allowed (✓) to excluded (×) compared to the previous analysis carried out in 2017 [25].

Type	I	II	LS	Flipped
$h_1 = h_{125}$	×	×	τ	$\underline{\times}$
$h_2 = h_{125}$	×	$\underline{\times}$	τ	×
$h_3 = h_{125}$	×	×	τ	×

The work is organized as follows. In Sec. II, we recapitulate the symmetries and resulting Lagrangian for the C2HDM, with the possible model choices for the Yukawa couplings. In Sec. III, we succinctly describe the status of the eEDM calculation in the C2HDM and the experimental bounds. In Sec. IV, we complete the list of constraints to be applied to this model, both theoretical and experimental ones, followed by the description of the adopted sampling strategy. Sections V and VI are devoted our results, the former focused on the case type II with $h_{125} = h_2$, and the latter on other cases. After summarizing our conclusions in Sec. VII, we present the details of on our application of HIGGSSIGNALS in Appendix A. As additional material we show the numerical evaluation of the diagrams that participate in the eEDM calculation for two points in parameter space in Appendix B.

II. THE C2HDM

In this work, we discuss an extension of the SM with a CP-violating scalar sector, with the addition of a scalar doublet with a softly broken $\mathbb{Z}_2$ symmetry, known as the C2HDM [6–14]. We follow the description of the model in Ref. [25] and write the scalar potential as

$$V = m_{11}^2|\Phi_1|^2 + m_{22}^2|\Phi_2|^2 - (m_{12}^2\Phi_1^\dagger\Phi_2 + \mathrm{H.c.}) + \frac{\lambda_1}{2}(\Phi_1^\dagger\Phi_1)^2 + \frac{\lambda_2}{2}(\Phi_2^\dagger\Phi_2)^2 + \lambda_3(\Phi_1^\dagger\Phi_1)(\Phi_2^\dagger\Phi_2) + \lambda_4(\Phi_1^\dagger\Phi_2)(\Phi_2^\dagger\Phi_1) + \left[\frac{\lambda_5}{2}(\Phi_1^\dagger\Phi_2)^2 + \mathrm{H.c.}\right], \quad (1)$$

where all couplings are real, except for m_{12}^2 and λ_5. The parameters of the scalar potential in Eq. (1) are thus defined in a basis where the softly broken $\mathbb{Z}_2$ symmetry is manifest and where the two scalar field vacuum expectation values are real and positive. Each of the doublets is written as an expansion around the real vacuum expectation values (vevs) of the neutral components $\langle\Phi_i^0\rangle = v_i/\sqrt{2}$ ($i = 1, 2$), with $v^2 = v_1^2 + v_2^2 \approx 246$ GeV,

$$\Phi_1 = \begin{pmatrix} \phi_1^+ \\ \frac{v_1+\rho_1+i\eta_1}{\sqrt{2}} \end{pmatrix} \quad \text{and} \quad \Phi_2 = \begin{pmatrix} \phi_2^+ \\ \frac{v_2+\rho_2+i\eta_2}{\sqrt{2}} \end{pmatrix}. \quad (2)$$

The minimum conditions can then be written as three equations,

$$m_{11}^2 v_1 + \frac{\lambda_1}{2}v_1^3 + \frac{\lambda_{345}}{2}v_1 v_2^2 = \mathrm{Re}(m_{12}^2)v_2, \quad (3)$$

$$m_{22}^2 v_2 + \frac{\lambda_2}{2}v_2^3 + \frac{\lambda_{345}}{2}v_1^2 v_2 = \mathrm{Re}(m_{12}^2)v_1, \quad (4)$$

$$2\,\mathrm{Im}(m_{12}^2) = v_1 v_2\,\mathrm{Im}(\lambda_5), \quad (5)$$

which, for nonzero vevs v_1 and v_2, ensure one independent *CP*-violating phase if $\mathrm{Im}\{\lambda_5^*(m_{12}^2)^2\} \neq 0$ [6,7,11]. In Eqs. (3) and (4), we have introduced the variable

$$\lambda_{345} = \lambda_3 + \lambda_4 + \mathrm{Re}(\lambda_5). \quad (6)$$

The diagonalization procedure starts with a rotation to the Higgs basis [71–74],

$$\begin{pmatrix} \mathcal{H}_1 \\ \mathcal{H}_2 \end{pmatrix} = R_H^T \begin{pmatrix} \Phi_1 \\ \Phi_2 \end{pmatrix} \equiv \begin{pmatrix} c_\beta & s_\beta \\ -s_\beta & c_\beta \end{pmatrix} \begin{pmatrix} \Phi_1 \\ \Phi_2 \end{pmatrix}, \quad (7)$$

with

$$\tan\beta \equiv \frac{v_2}{v_1}. \quad (8)$$

The doublets in the Higgs basis can then be written, with the Goldstone bosons $G^\pm$ and G^0 in $\mathcal{H}_1$, as

$$\mathcal{H}_1 = \begin{pmatrix} G^\pm \\ \frac{1}{\sqrt{2}}(v + H^0 + iG^0) \end{pmatrix} \quad \text{and} \quad \mathcal{H}_2 = \begin{pmatrix} H^\pm \\ \frac{1}{\sqrt{2}}(R_2 + iI_2) \end{pmatrix}. \quad (9)$$

The mass matrix for the neutral Higgs states is defined for ρ_1, ρ_2, and $\rho_3 = I_2$ as,

$$(\mathcal{M}^2)_{ij} = \left\langle \frac{\partial^2 V}{\partial\rho_i \partial\rho_j} \right\rangle, \quad (10)$$

which can be diagonalized by a general orthogonal matrix R [15]. That is,

$$R\mathcal{M}^2 R^T = \mathrm{diag}(m_1^2, m_2^2, m_3^2), \quad (11)$$

for which we follow the choice

$$R = \begin{pmatrix} c_1 c_2 & s_1 c_2 & s_2 \\ -(c_1 s_2 s_3 + s_1 c_3) & c_1 c_3 - s_1 s_2 s_3 & c_2 s_3 \\ -c_1 s_2 c_3 + s_1 s_3 & -(c_1 s_3 + s_1 s_2 c_3) & c_2 c_3 \end{pmatrix}, \quad (12)$$

with the notation $s_i \equiv \sin\alpha_i$, $c_i \equiv \cos\alpha_i$ ($i = 1, 2, 3$), in the ranges

$$-\pi/2 < \alpha_1 \leq \pi/2, \quad -\pi/2 < \alpha_2 \leq \pi/2, \quad -\pi/2 < \alpha_3 \leq \pi/2. \quad (13)$$

The model contains three neutral particles with no definite *CP* quantum numbers, h_1, h_2 and h_3, and two charged scalars $H^\pm$. The masses for the neutral Higgs bosons are ordered such that $m_1 \leq m_2 \leq m_3$. The set of independent parameters of the potential sector can be chosen as

$$\tan\beta, m_{H^\pm}, \alpha_1, \alpha_2, \alpha_3, m_1, m_2, \mathrm{Re}(m_{12}^2). \quad (14)$$

With this choice, the mass of the heaviest neutral scalar is a derived quantity, obeying

$$m_3^2 = \frac{m_1^2 R_{13}(R_{12}\tan\beta - R_{11}) + m_2^2 R_{23}(R_{22}\tan\beta - R_{21})}{R_{33}(R_{31} - R_{32}\tan\beta)}. \quad (15)$$

Here, m_3^2 has to be a positive quantity, which is implemented in the optimization algorithm as a constraint that must be satisfied before the fitting procedure is initiated [58,75,76].

The imposed $\mathbb{Z}_2$ symmetry is motivated by the possibility of forbidding tree-level flavor-changing neutral couplings known to be very constrained experimentally. The adopted natural flavour conservation mechanism [4,5] extends the symmetry to the Higgs-fermion Yukawa sector

TABLE II. Yukawa couplings of the Higgs bosons h_i in the C2HDM, divided by the corresponding SM Higgs couplings. The expressions correspond to $[c^e(h_i ff) + ic^o(h_i ff)\gamma_5]$ from Eq. (16).

	Up-type	Down-type	Leptons
Type I	$\frac{R_{i2}}{s_\beta} - i\frac{R_{i3}}{t_\beta}\gamma_5$	$\frac{R_{i2}}{s_\beta} + i\frac{R_{i3}}{t_\beta}\gamma_5$	$\frac{R_{i2}}{s_\beta} + i\frac{R_{i3}}{t_\beta}\gamma_5$
Type II	$\frac{R_{i2}}{s_\beta} - i\frac{R_{i3}}{t_\beta}\gamma_5$	$\frac{R_{i1}}{c_\beta} - it_\beta R_{i3}\gamma_5$	$\frac{R_{i1}}{c_\beta} - it_\beta R_{i3}\gamma_5$
Lepton specific	$\frac{R_{i2}}{s_\beta} - i\frac{R_{i3}}{t_\beta}\gamma_5$	$\frac{R_{i2}}{s_\beta} + i\frac{R_{i3}}{t_\beta}\gamma_5$	$\frac{R_{i1}}{c_\beta} - it_\beta R_{i3}\gamma_5$
Flipped	$\frac{R_{i2}}{s_\beta} - i\frac{R_{i3}}{t_\beta}\gamma_5$	$\frac{R_{i1}}{c_\beta} - it_\beta R_{i3}\gamma_5$	$\frac{R_{i2}}{s_\beta} + i\frac{R_{i3}}{t_\beta}\gamma_5$

such that each of the three families of fermions couples to one and only one scalar field. Introducing the up-, down- and lepton-type fermion doublets as Φ_u, Φ_d and Φ_ℓ, for the doublet Φ_i ($i = 1, 2$) that respectively couples to up-type, down-type and charged leptons, there are four possible Yukawa types of the softly broken $\mathbb{Z}_2$ symmetric 2HDM:

(i) Type I: $\Phi_u = \Phi_d = \Phi_\ell \equiv \Phi_2$
(ii) Type II: $\Phi_u \equiv \Phi_2 \neq \Phi_d = \Phi_\ell \equiv \Phi_1$
(iii) Lepton-specific (LS) $\Phi_u = \Phi_d \equiv \Phi_2 \neq \Phi_\ell \equiv \Phi_1$
(iv) flipped $\Phi_u = \Phi_\ell \equiv \Phi_2 \neq \Phi_d \equiv \Phi_1$.

The Yukawa Lagrangian for the neutral scalars can be written as

$$\mathcal{L}_Y = -\sum_{i=1}^{3} \frac{m_f}{v} \bar{\psi}_f [c^e(h_i ff) + ic^o(h_i ff)\gamma_5]\psi_f h_i, \tag{16}$$

where ψ_f denote the fermion fields with mass m_f. The coefficients of the CP-even and of the CP-odd part of the Yukawa coupling, $c^e(h_i ff)$ and $c^o(h_i ff)$, are presented in Table II and will be abbreviated by c_f^e and c_f^o, respectively, for the state identified as the 125 GeV scalar. The different families of fermions are identified by choosing f with the labels t, b and τ for up-type, down-type and leptons, respectively.

The aim of our simulations is to study the CP nature of the 125 GeV scalar, identified out of the three h_i as h_{125}, with a focus on the possibility of large pseudoscalar c_f^o couplings. There are experimental bounds on the CP-odd (c_t^o) versus CP-even (c_t^e) couplings to the top quark [77]:

$$|\theta_t| = |\arctan(c_t^o/c_t^e)| < 43° \quad \text{at } 95\%\text{CL}. \tag{17}$$

In more recent LHC data analyses, bounds were also placed on the CP-odd (c_τ^o) versus CP-even (c_τ^e) couplings to the tau lepton [56,78]:

$$|\theta_\tau| = |\arctan(c_\tau^o/c_\tau^e)| < 34° \quad \text{at } 95\%\text{CL}. \tag{18}$$

There are no direct bounds on the CP-odd coupling to the bottom quark (c_b^o). Reference [29] found the situation summarized in Table I.

The Higgs couplings to the massive gauge bosons $V = W, Z$ are given by

$$ig_{\mu\nu} c(h_i VV) g_{h^{\rm SM}VV}, \tag{19}$$

with the SM coupling $g_{h^{\rm SM}VV}$ given by gM_W for the $V = W$ case and $gM_Z/\cos\theta_W$ for $V = Z$, where $h^{\rm SM}$ denotes the SM Higgs. Since the signs of c_f^e and c_f^o have no absolute meaning and are relative to the sign of $k_V \equiv c(h_{125}VV)$, our results are shown with combinations of $\text{sign}(k_V)c_f^o$ vs $\text{sign}(k_V)c_f^e$.

III. THE ELECTRON EDM

We now turn to a discussion of the eEDM (the contributions from the muon EDM and from nonleptonic EDMs are currently less stringent and thus not considered [25]). For the theoretical predictions, we use the formulas in Refs. [12,22,36,43,47,79]. We stress that the calculation as presented in Refs. [36,47] includes the complete set of nonvanishing contributions to the eEDM in the C2HDM. Although this complete set corresponds to a gauge-independent result, the individual contributions depend in general on the gauge. In this work, after explicitly checking that their sum is gauge independent, we choose the Feynman gauge for these individual contributions. We investigate for the first time the role of the kite diagrams [36], shown in Fig. 1, in simulations of the parameter space of the C2HDM satisfying all theoretical and most recent experimental constraints. As discussed above, we also assess the impact of Barr-Zee diagrams with the charm quark (hereafter referred to as charm diagrams). Finally, we comment on diagrams that yield even smaller contributions.

Beyond the question of which diagrams are included, the two-loop eEDM calculation also involves the choice of the renormalization scheme. In particular, different approaches can be adopted for the renormalization prescriptions of the fermion masses. The most common choices are $\overline{\rm MS}$ running masses at the scale M_Z $[\bar{m}_t(M_Z), \bar{m}_b(M_Z)]$ [22,36,80], or pole mass for the top quark in combination with the running bottom-quark mass at the scale $\bar{m}_b$ $[m_t, \bar{m}_b(\bar{m}_b)]$ [25,31,38,81].[1] For brevity, in what follows we refer to the first choice as the "M_Z-masses" scheme and to the second as the "pole-masses" scheme. In Ref. [29] it was shown that in the type II model with the choice $h_2 = h_{125}$, the choice of the renormalization scheme adopted for the fermion masses in the eEDM calculation is relevant. Using the M_Z-masses scheme, it was found that sizable CP-odd components in the $h_{125}b\bar{b}$ coupling were incompatible with the combined experimental constraints from the upper limit

[1]For the tau lepton, we always use the pole mass, m_τ. The same choice was made in Ref. [29]; however, that reference contains a typo, as it states that two mass schemes were considered for that particle.

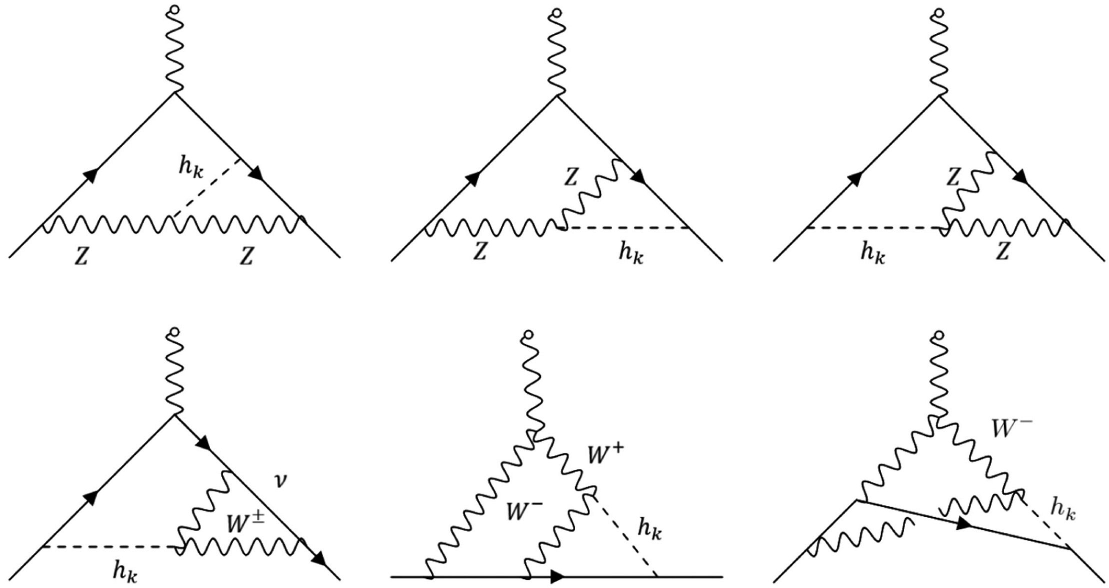

FIG. 1. Generic diagrams of the kite class. Top row: neutral current contributions. Bottom row: charged current contributions.

on the eEDM and from cross-section limits from BSM scalar searches. For the pole-masses scheme, by contrast, there remained the possibility of considerable large pseudoscalar components of the Higgs-fermion couplings. In Sec. V, we will review this discussion in light of the updated eEDM calculation with kite contributions.

IV. SAMPLING

A. Theoretical and experimental constraints

With the aim of probing the *CP* nature of the 125 GeV scalar, we perform an extensive scan of the parameter space subject to both theoretical and experimental constraints. In addition to the eEDM calculation described in the previous section, the imposed theoretical requirements include boundedness from below of the scalar potential [82–84], the enforcement of a global electroweak minimum through the discriminant condition that avoids metastable vacua [85], and perturbative unitarity [86–88]. The effects of new physics on electroweak precision observables are evaluated through the oblique parameters S, T and U [89,90], which are required to agree at the 2σ level with the global electroweak fit of Ref. [91].

Constraints from Higgs precision measurements are imposed by requiring agreement with the LHC determinations of coupling modifiers [92] at 3σ and signal strengths [93] at 2σ, consistent with CMS data [94], for each individual initial-state $\times$ final-state production channel. Direct searches for additional scalar states are taken into account by implementing the C2HDM in the software framework HIGGSTOOLS (HT), version 1.1.3 [95], and running the most recent module HIGGSBOUNDS (HB), version 1.7.

Flavor constraints are incorporated through an explicit calculation of the $b \to s\gamma$ process following Ref. [96], requiring agreement with the experimental measurement [97] at the 3σ level. As shown in Refs. [98–102], this observable implies the lower bound $m_{H^+} > 580$ GeV at 95% CL (2σ) in the type II C2HDM. The global fit of Ref. [103] confirms this lower bound, and shows that it also holds for the flipped model.

Constraints from direct LHC searches for *CP* violation of the Higgs boson are applied after those from Higgs precision measurements discussed above. Specifically, for the *CP*-violating couplings of h_{125} to the top quark, we impose the bounds given in Eq. (17) [77]. As for the bounds on the *CP*-violating couplings of h_{125} to the tau lepton (for short, bounds on θ_τ), we investigate two alternative approaches: either including the likelihood estimate given by the module HIGGSSIGNALS (HS) within HT [95], or considering Eq. (18) [56,78]. Concerning the former, a comment is in order. When sampling the parameter space subject to all the constraints described above (with the bounds on θ_τ implemented via the public version of the HS module), we rapidly encounter a regime in which all points exhibiting sizable pseudoscalar Higgs-fermion couplings are excluded by HS. In Appendix A, we explain in detail the origin of this tension, and how we modified the dataset used by HS to address this issue. In what follows, whenever we consider the HS to impose bounds on θ_τ, we always use the modified dataset. A more detailed discussion is provided in Appendix A.

B. Sampling techniques

In our results, we shall be mainly interested in the type II and flipped models. For a generic assignment of h_i to h_{125}, the sampling regions can be presented in a compact way for both models. As SM input values, we take

$$\begin{array}{llll} G_F & = 1.16638\times 10^{-5}\,\mathrm{GeV}^{-2} & M_Z & = 91.1876\,\mathrm{GeV} \\ \alpha_{\mathrm{em}}^{-1}(M_Z) & = 127.92 & M_W & = 80.385\,\mathrm{GeV} \\ \alpha_{\mathrm{em}}^{-1} & = 137.035999 & m_\tau & = 1.77682\,\mathrm{GeV} \\ m_t & = 172.5\,\mathrm{GeV} & \bar{m}_t(M_Z) & = 163\,\mathrm{GeV} \\ \bar{m}_b(\bar{m}_b) & = 4.7800\,\mathrm{GeV} & \bar{m}_b(M_Z) & = 2.88\,\mathrm{GeV} \\ \Gamma_W & = 2.08430\,\mathrm{GeV} & \Gamma_Z & = 2.49427\,\mathrm{GeV} \end{array} \tag{20}$$

After setting $m_{125} = 125.09$ GeV, we write the sampling of the independent parameters as

$$\begin{gathered} m_{1<h_{125}} \in [15.0, 122.5]\ \mathrm{GeV}; \qquad m_{2>h_{125}} \in [127.5, 1000]\ \mathrm{GeV}; \qquad m_{H^\pm} \in [580, 1000]\ \mathrm{GeV}; \\ \tan\beta \in [0.3, 30.0]; \qquad \mathrm{Re}(m_{12}^2) \in [\pm 10^{-1}, \pm 10^7]; \qquad \alpha_1, \alpha_2, \alpha_3 \in \left[-\frac{\pi}{2}, \frac{\pi}{2}\right]. \end{gathered} \tag{21}$$

However, a purely random sampling of the parameter space is highly inefficient in identifying configurations with large pseudoscalar fermion-Higgs couplings. As discussed above, the mass parameter m_3^2 is a derived quantity and it can become negative in parts of the sampled space. These points must be discarded as they are unphysical. In addition, for the choice $h_2 \equiv h_{125}$ the heavy neutral scalar is further required to be approximately degenerate in mass with the charged Higgs in order to comply with experimental constraints [104]. Still, obtaining an experimentally viable solution in the resulting reduced parameter region is a slow process.

We therefore adopt two complementary strategies, which we label strategy 1 and strategy 2 in the following. In the first, we perform a guided scan in which the parameter space is explored close to the phenomenological boundary, iteratively increasing the pseudoscalar component of the Higgs-fermion couplings [25,29,57]. In the second, we employ an AI-based black-box optimization technique, originally introduced in Ref. [69], subsequently applied to a real 3HDM in Ref. [70], and later extended to 3HDMs with explicit CP violation in the scalar sector [58,76].

In strategy 1, the sampling is initiated from points for which the squared mass of the third neutral scalar is already physical. In contrast, the ML method of strategy 2—which does not rely on preexisting training data—implements a hierarchical optimization procedure in which the positivity of the squared mass is enforced as a hard constraint within the loss function. Only after this requirement is satisfied does the algorithm proceed to optimize the remaining theoretical and experimental constraints [58,75,76].

Strategy 2 consists of writing the validation of points given all constraints as a black-box optimization problem and applying an evolutionary strategy. Compared to alternatives, a major advantage of this method is that no initial sampled data is needed. For each individual observable or constrained quantity $\mathcal{O}$, a function $C(\mathcal{O})$ is introduced as

$$C(\mathcal{O}) = \max(0, -\mathcal{O} + \mathcal{O}_{LB}, \mathcal{O} - \mathcal{O}_{UB}), \tag{22}$$

where $\mathcal{O}_{LB}, \mathcal{O}_{UB}$ are the allowed lower and upper bounds for the respective quantity. The function $C(\mathcal{O})$ returns 0 only if $\mathcal{O}$ lies within the specified interval; otherwise, it returns a positive number quantifying *how far* the value of the observable is from the specified bounds. All the constraint functions are then encapsulated into a single loss function,

$$L(\theta) = \sum_{i=1}^{N_c} C(\mathcal{O}_i(\theta)), \tag{23}$$

which is used as the search objective. The sampling algorithm employed in strategy 2 is the covariant matrix adaptation evolutionary strategy (CMA-ES) [105,106]. In CMA-ES, the distribution is a highly localized multivariate normal, from which a generation of candidate solutions is sampled and their losses evaluated using Eq. (23). The candidates are then ranked from best to worst, indicating how close they are to fulfilling the sum of all constraint functions, with the best candidates used to compute a new mean and approximate the covariance matrix.

By construction, individual CMA-ES runs are statistically independent: each run is initialized with a new choice of the mean vector and covariance matrix, and the optimization proceeds using only the information generated within that run. While this fully blind initialization ensures independence, it was found to lead to an uneven coverage of the parameter space, with distinct regions being explored in isolation and the overall sampling density remaining sparse in intermediate domains. To mitigate this limitation and improve the continuity and efficiency of the exploration, CMA-ES also allows for initialization using the mean

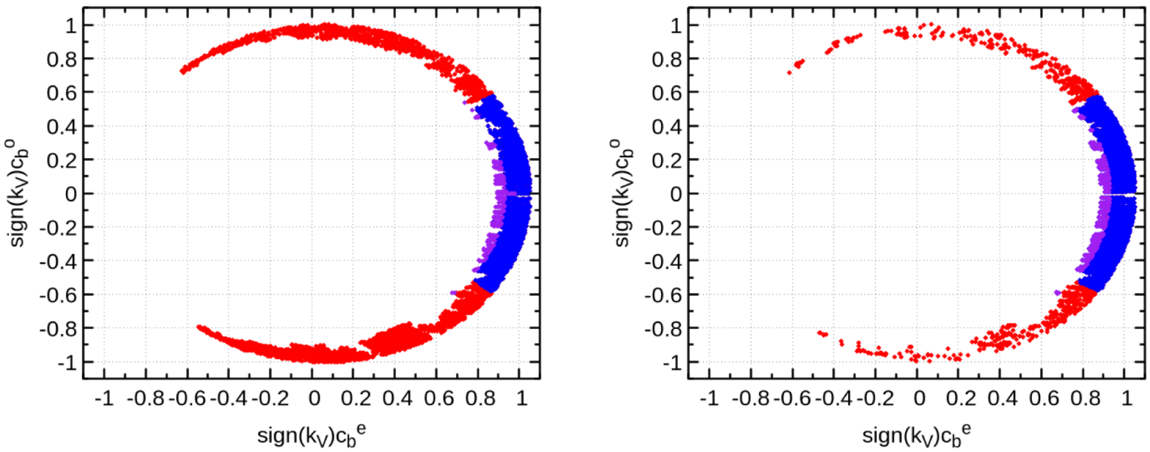

FIG. 2. Points on the plane $\mathrm{sign}(k_V)c_b^o$ vs $\mathrm{sign}(k_V)c_b^e$ obtained with strategy 1 in the type II C2HDM with $h_{125} = h_2$. The purple (blue) points include all constraints, including those relative to θ_τ implemented via HS [via Eq. (18)], while the red points include all constraints except those relative to θ_τ. Left panel: current eEDM limit 4.1×10^{-30} e.cm. Right panel: projected eEDM limit 1.0×10^{-33} e.cm. See text for details.

vector and covariance matrix obtained from previous optimization runs, hereafter referred to as *seeded runs*. When combined with an integrated anomaly-detection–based novelty reward mechanism, implemented via a histogram-based outlier score (HBOS) [107] evaluated on a selected subset of parameters or observables of interest, this strategy yields a more uniform and coherent exploration of the model's parameter space and its associated physical implications. Over the range of allowed values, HBOS constructs a histogram of equal-width bins for each parameter dimension. The frequency of samples that fall into each bin is used as an estimate for the density. The points with higher density, similar to previously explored points in parameter/observable space, receive larger penalties in the modified loss function.

We conclude this section with two final remarks. First, all datasets used to produce the plots in this paper—under both strategy 1 and strategy 2—are generated by imposing all constraints described in Sec. IV A, with the exception of those associated with θ_τ. As discussed at the end of Sec. IV A, two alternative implementations of the θ_τ constraints are considered; hence, whenever these constraints are imposed, we explicitly state which alternative is adopted. Second, all plots presented in this work that rely on strategy 2 are based on samples containing at least $\mathcal{O}(10^7)$ points. The strong EDM bound is fed as an objective to the optimization algorithm in strategy 2. Thus, the iterative procedure will attempt to find the necessary and strong cancellations required to meet the current experimental bound.

V. RESULTS FOR TYPE II WITH $h_2 = h_{125}$

Motivated by the discussion above on the choice of the fermion-mass renormalization schemes in the eEDM calculation, we focus in this section on the type II model with $h_2 \equiv h_{125}$. Besides the usual Barr-Zee diagrams [43–46] (whose diagrams with fermion loops include only third generation fermions), we start by including only the kite diagrams in our eEDM calculation. This study is carried out in Secs. V A and V B, which implement strategy 1 and strategy 2, respectively. At the end of Sec. V B, we discuss the role of the contributions of other diagrams to the eEDM. In Sec. V C, we then turn to a specific region of the parameter space characterized by small values of the scalar mass m_1. Finally, Sec. V D is devoted to a detailed investigation of the role played by the charm diagrams in the eEDM calculation.

A. Phenomenology with strategy 1

Figure 2 shows two plots of the plane $\mathrm{sign}(k_V)c_b^o$ vs $\mathrm{sign}(k_V)c_b^e$ generated with strategy 1, imposing the current eEDM limit (left) and imposing a projected eEDM limit 1.0×10^{-33} e.cm [51–53] (right). In the calculation of the eEDM in both panels, the M_Z masses are used and, as discussed above, only the usual Barr-Zee diagrams and the kite diagrams are included. The red points correspond to parameter points that fulfill all constraints discussed in Sec. IV except those on θ_τ, while the purple points additionally impose those constraints using HS. The figure shows that, for both eEDM scenarios considered in the panels, the dominant limitation on the magnitude of the pseudoscalar component of h_{125} arises from the bounds on θ_τ. The figure also shows that the valid (purple) points are all close to the SM solution $(\mathrm{sign}(k_V)c_b^e, \mathrm{sign}(k_V)c_b^o) = (1, 0)$; in particular, no points can be found close to the so-called "wrong-sign" solution $(\mathrm{sign}(k_V)c_b^e, \mathrm{sign}(k_V)c_b^o) = (-1, 0)$. Finally, we confirm that the points sampled are in agreement with the public code SCANNERS [108,109], now also updated to include the kite diagrams in the eEDM calculation.

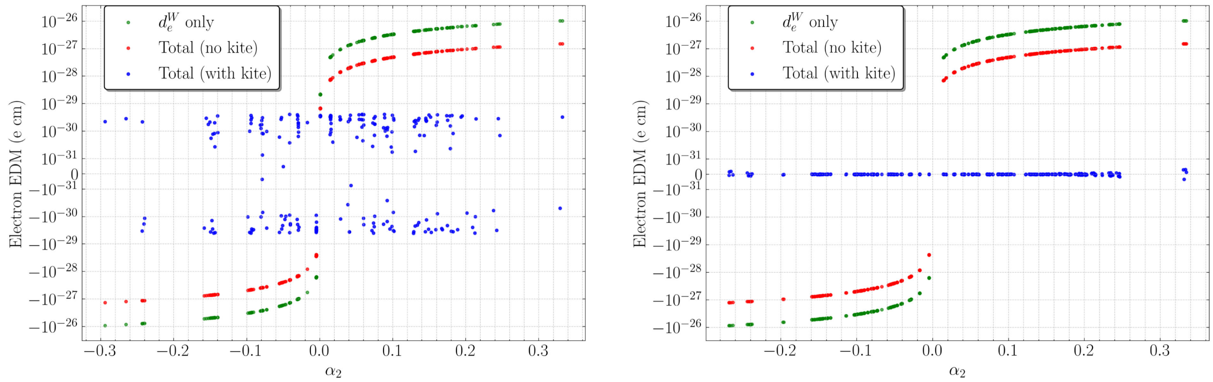

FIG. 3. Different contributions to the eEDM for the set of points sampled: total contribution (blue), total contribution except for the kite diagrams (red), contribution of the dominant class of diagrams (green). Left panel: current eEDM limit 4.1×10^{-30} e.cm. Right panel: projected eEDM limit 1.0×10^{-33} e.cm.

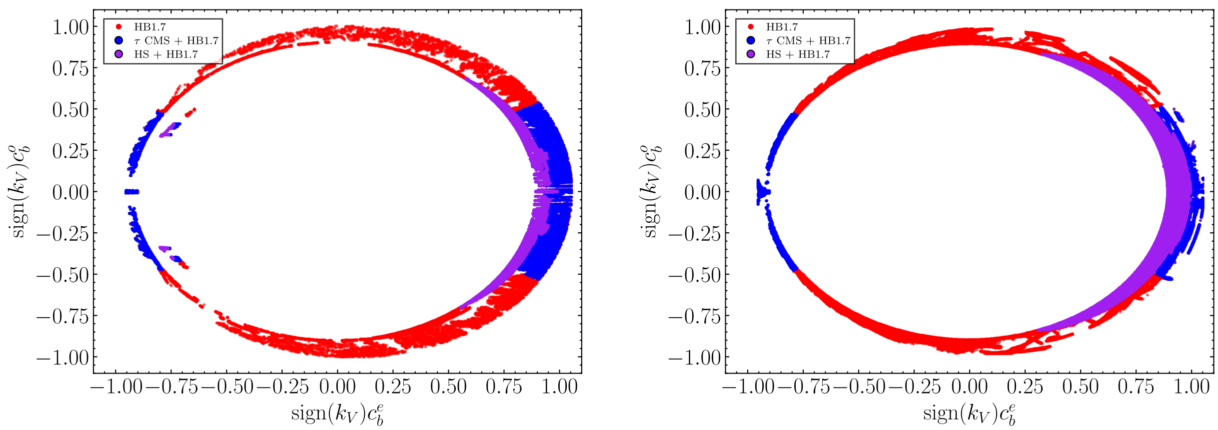

FIG. 4. Points on the plane $\mathrm{sign}(k_V)c_b^o$ vs $\mathrm{sign}(k_V)c_b^e$ obtained with strategy 2 in the type II C2HDM with $h_{125} = h_2$. Red points pass all constraints except those on θ_τ; the remaining points additionally impose the latter constraint: either via HS (in purple) or via Eq. (18) (in blue). Left: eEDM calculated in the M_Z-masses scheme. Right: eEDM calculated in the pole-masses scheme.

In Fig. 3, we assess the impact of the kite diagrams on the eEDM prediction. The blue points show the total predicted value of the eEDM, the red ones correspond to the same prediction with the kite-diagram effects subtracted, and the green points represent the class of diagrams yielding the largest contribution to the eEDM for each sampled parameter point. From this comparison, we confirm the result of Ref. [36] that the inclusion of the kite diagrams induces $\mathcal{O}(1)$ corrections to the eEDM prediction for the dataset sampled. Both panels of Fig. 3 also show that, except for very small values of α_2, there are large cancellations between the different contributions to the eEDM.

B. Phenomenology with strategy 2

As mentioned in the Introduction, standard scans can completely miss certain valid regions of the parameter space—regions where new phenomenology may be possible. Having discussed in the previous section the values found on the plane $\mathrm{sign}(k_V)c_b^o$ vs $\mathrm{sign}(k_V)c_b^e$ with the standard scans of strategy 1, we now turn to ML techniques. The datasets considered below include optimization runs seeded with a subset of points obtained from earlier unseeded runs. The simulations are designed to determine the maximal allowed size of the *CP*-odd fermionic coupling, imposing the bounds on θ_τ either through HS or through Eq. (18). All optimization runs incorporate a novelty-reward mechanism targeting large *CP*-odd fermion couplings.

The results are shown in Fig. 4. As before, the calculation of the eEDM is performed including the usual Barr-Zee diagrams and the kite diagrams. We now differentiate the eEDM calculation performed with the M_Z-masses scheme (left panel) from the calculation performed with the pole-masses scheme (right panel).[2] Points shown in red satisfy all constraints described in Sec. IV, with the exception of those on θ_τ. The remaining points additionally impose the latter bounds: either via HS (in purple) or via

[2]For the definition of the M_Z-masses and the pole-masses scheme, cf. Sec. III.

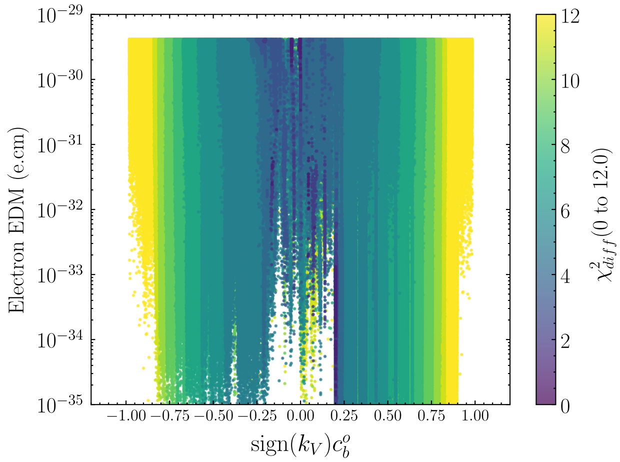

FIG. 5. Points obtained with strategy 2 in the type II C2HDM with $h_{125} = h_2$, on the plane eEDM prediction (calculated with the pole-masses scheme) vs $\mathrm{sign}(k_V)c_b^o$. The color code shows the lowest possible χ^2 calculated with HS.

Eq. (18) (in blue). This figure should be directly compared with Fig. 2. Several noteworthy features emerge from this comparison.

First, Fig. 4 clearly demonstrates the substantial advantage of the ML-based search over the standard scanning strategy of Fig. 2. The ML approach uncovers a significantly larger region of parameter space with large *CP*-odd couplings. In particular, it reveals a viable region in the vicinity of the wrong-sign solution—which, as noted above, is entirely absent in the standard scan.

Second, the qualitative features of the ML results are similar for both M_Z-masses and pole-masses schemes. Dedicated tests show that this similarity disappears once the kite diagrams are excluded, in agreement with the findings of Ref. [29] (see, in particular, the comparison between the right panel of Fig. 1 and the left panel of Fig. 2 therein). This provides further confirmation of the central role of the kite diagrams, as previously emphasized in Ref. [36]. Their importance is not unexpected, given that, as discussed before, these diagrams are required to ensure gauge invariance of the eEDM calculation [36]. As a consequence, non-negligible values of $|c_b^o|$ in the type II C2HDM with $h_{125} \equiv h_2$ are found to be phenomenologically viable, constrained primarily by the measurements of θ_τ.

Third, Fig. 4 illustrates the impact of the two different implementations of the θ_τ constraint. The blue points cover the same width of the ellipse as the red points, but they stop abruptly for $|\theta_\tau| \geq 34°$ due to the constraint of Eq. (18). The region covered by the purple points, by contrast, has a narrower width than the red points, and they are not constrained by the abrupt cut at $|\theta_\tau| = 34°$. Both these features result from the likelihood estimate given by HS.

Finally, in the M_Z-masses scheme shown in the left panel of Fig. 4, we observe isolated regions near $|c_b^o| \sim 0.4$ and $\mathrm{sign}(k_V)c_b^e \sim -0.75$ that are absent in the pole-masses scheme displayed in the right panel. These points correspond to comparatively light scalar masses, $m_1 \sim 50$ GeV. We return to a detailed discussion of this region in Sec. V C below.

An interesting question concerns the possibility of accommodating increasingly stringent eEDM bounds while still obtaining parameter points with the largest $|c_b^o|$ components compatible with current experimental constraints. This issue is illustrated in Fig. 5.[3] The plot shows that, irrespective of how stringent the eEDM bound becomes—even down to 10^{-35} e.cm—it is always possible to identify regions of parameter space that allow for sizable $|c_b^o|$ components, provided the parameters are tuned so that large cancellations conspire to satisfy progressively stronger eEDM constraints.

Although not shown explicitly, we also performed dedicated runs that led to further observations. First, percent-level variations in the input mass values still permit the identification of parameter sets for which the required cancellations to satisfy the eEDM bounds occur. It is found, however, that such small changes require significant changes in the remaining input parameters in order to still fulfill the required cancellations. This behavior is not unexpected, given that the cancellations involve contributions from very different diagrams. Second, once the eEDM sensitivity reaches the level of 10^{-33} e.cm, the contributions of several types of diagrams not included so far in our eEDM calculation (such as Barr-Zee diagrams with quarks beyond the third generation, as well as one-loop diagrams) become numerically relevant.

C. Isolated regions with small h_1 masses

As discussed above, the isolated regions located around $|c_b^o| \sim 0.4$ and $\mathrm{sign}(k_V)c_b^e \sim -0.75$ in the plot with the M_Z-masses scheme of Fig. 4 (left panel) correspond to scenarios with small scalar masses, $m_1 \sim 50$ GeV. We probe this feature in more detail in Fig. 6, which displays the subset of points from the left panel of Fig. 4 with $m_1 < 60$ GeV. The figure reveals a region close to the SM-like point $(\mathrm{sign}(k_V)c_b^e, \mathrm{sign}(k_V)c_b^o) = (1, 0)$, as well as an isolated region near $|c_b^o| \sim 0.4$ and $\mathrm{sign}(k_V)c_b^e \sim -0.75$.

[3]As before, the calculation of the eEDM is performed including the usual Barr-Zee diagrams and the kite diagrams, assuming the pole-masses scheme. Furthermore, and as usual, the plot is generated from datasets satisfying all constraints described in Sec. IV A except those on θ_τ. On the other hand, the figure does not commit to a specific prescription for imposing the θ_τ constraints. If one adopts the alternative based on Eq. (18), only the points lying within the range of $\mathrm{sign}(k_V)c_b^o$ spanned by the blue points in the right panel of Fig. 4 are considered valid. If, instead, the HS alternative is followed, the color coding of the figure, representing the χ^2_{diff} obtained from HS, allows the θ_τ constraint to be imposed at the desired confidence level within that framework.

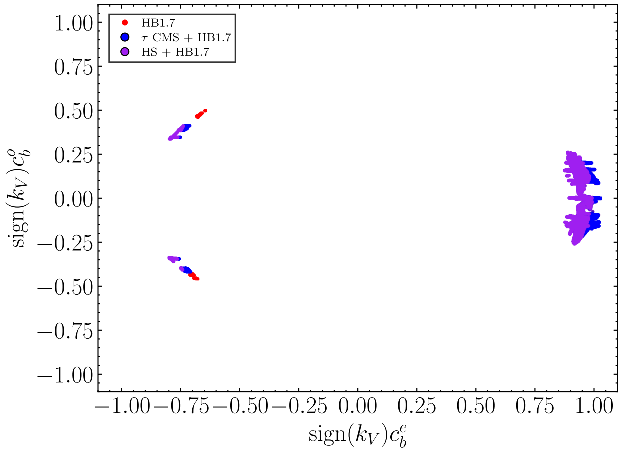

FIG. 6. The same as the left panel of Fig. 4, but considering exclusively points with $m_1 \leq 60$ GeV.

This latter region is disconnected from the vicinity of the wrong-sign solution $(\mathrm{sign}(k_V)c_b^e, \mathrm{sign}(k_V)c_b^o) = (-1, 0)$, for which no parameter points with small m_1 masses survive. In fact, the isolated region corresponds to a very narrow mass window, 51 GeV $\lesssim m_1 \lesssim$ 53 GeV.

We note that the analogous plot obtained using the pole-masses scheme does not exhibit these isolated regions. This behavior is easy to understand. As discussed above, the parameter regions compatible with the eEDM constraints arise from very precise cancellations among different diagrammatic contributions, typically at the per-mil level. Thus, small variations in the input mass parameters lead to large shifts in the remaining parameter space, making it unsurprising that a narrow region present for the M_Z-masses scheme disappears for the pole-masses scheme.

To investigate the range of values taken by m_1, Fig. 7 displays all points shown in Fig. 4, now projected onto the plane $\mathrm{sign}(k_V)c_b^o$ versus m_1. Intermediate values of m_1 are excluded by HB through direct searches for additional Higgs bosons, as reported in Refs. [110–112]. From the left panel, one observes side bands with $|c_b^o| > 0.3$ clustered around $m_1 \sim 50$ GeV, corresponding to the isolated regions previously identified in Figs. 4 (left) and 6. These regions lie close to the current exclusion boundary. Given the strong sensitivity of these features to the precise input parameters, we do not attribute particular physical significance to the isolated regions appearing when the fermion masses are defined in the M_Z-masses scheme.

D. The charm diagrams

Up to now, we included in our calculations for the eEDM the new kite diagrams from Ref. [36], besides the usual Barr-Zee diagrams (which, we recall, contain only fermions of the third generation). One could wonder whether a Barr-Zee diagram with an intermediate charm quark would be important given the current experimental bounds. As we will now show, this is indeed the case, despite their mass suppression.

We have taken some of the points in the left panel of Fig. 4, which obey the current eEDM bounds and which were calculated *without* taking into consideration the charm diagrams; we then calculated, for those points, what the contribution of the charm diagrams would be. For the charm quark, we chose the running $\overline{\mathrm{MS}}$ mass $\bar{m}_c$ at the scale $\bar{m}_c$, namely $\bar{m}_c(\bar{m}_c) = 1.2$ GeV [113]. The result is shown in Fig. 8, which displays separately the contributions from the dominant class of diagrams (green), the kite diagrams (pink) and the charm diagrams (red). As was already discussed in the context of Fig. 3, it is clear that the kite diagrams are crucial for the cancellation. The plot also shows that the charm contribution comes in at the order of a few times 10^{-29} e.cm, well above the current experimental level of 4.1×10^{-30} e.cm [50]. Thus, it spoils the cancellation, and the points become disallowed.

Of course, although the charm contributions spoil the cancellation of points obtained without it, new points can be found which, when including the charm contribution, produce new precise cancellations, in line with the experimental bound. Thus, we have performed a new simulation

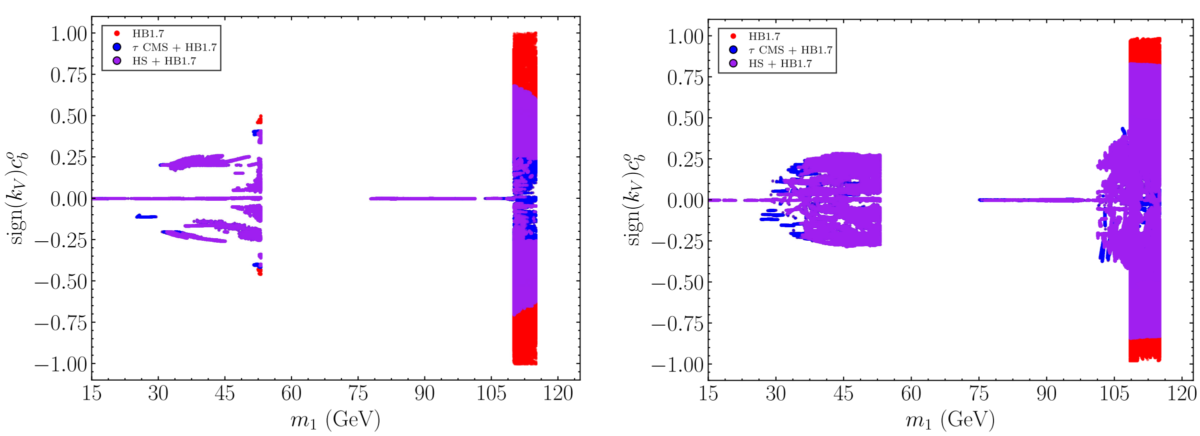

FIG. 7. The same as in Fig. 4, but for the plane $\mathrm{sign}(k_V)c_b^o$ vs m_1.

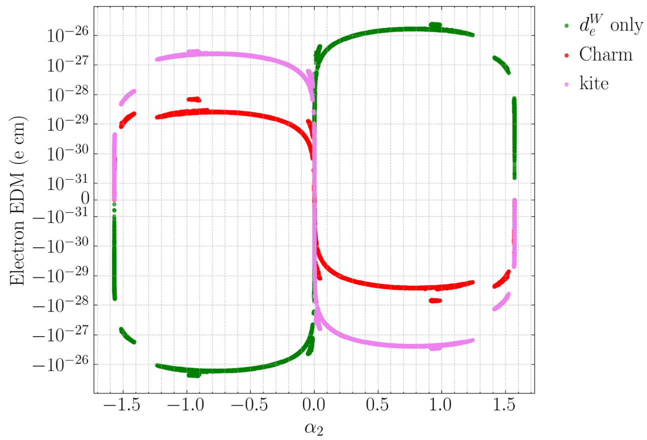

FIG. 8. Points of the left panel of Fig. 4, now projected on the plane eEDM vs α_2. Besides the contributions from the kite diagrams (pink) and the dominant diagrams (green), both of which were included in the calculation of the eEDM in Fig. 4, the plot also shows the contribution of the charm diagrams (red).

including both kite and charm contributions, shown in Fig. 9. In the left panel, we show the results in the above defined M_Z-masses scheme and with the charm-quark mass chosen as $\bar{m}_c(\bar{m}_c) = 1.2$ GeV. The right panel displays results obtained in the pole-masses scheme with the on-shell charm quark mass chosen as $m_c = 1.51$ GeV [114]. Comparing this figure (which includes the charm diagrams) with Fig. 4 (which does not), we see that all the features discussed previously remain. In conclusion, including the charm contributions alters the set of valid points obtained, but it does not preclude compliance with the current eEDM experimental bounds, nor does it alter the qualitative c_b^o features.

VI. REVISITING OTHER CASES OF THE C2HDM

Having established the importance of both kite and charm contributions to the eEDM, we revisit all scenarios listed in Table I using ML techniques (Strategy 2). In the type I model, the *CP*-odd couplings of all fermions are universal and are therefore strongly constrained by the top-quark sector, forcing them to remain very close to their SM values for all choices of mass ordering. We further verify that no viable solutions with large $|c_b^o|$ components exist in the type II and flipped models with $h_3 = h_{125}$, in agreement with the conclusions of Ref. [25].

We also find no viable points with large $|c_b^o|$ for the mass choice $h_1 = h_{125}$. This is shown for type II and flipped in Fig. 10, and the limitation is due to a combination of searches for heavy resonances [115–117], which is checked by HT. Nevertheless, the recent Ref. [118] makes the point that there may be some large *CP*-violating signals in type II with $h_1 = h_{125}$.

A few remarks are in order. First, looking at Fig. 13 in Ref. [118], we agree that indeed there are no large $|c_b^o|$ couplings (for h_{125}). Second, even when $s_2 = 0$ (implying that h_1 is a pure scalar), Ref. [11] points out in their endnote 20 that there will still be *CP* violation in the heavier scalars, proportional to $J_1 \propto (m_1^2 - m_2^2)(m_1^2 - m_3^2)(m_2^2 - m_3^2) \cos(\beta - \alpha_1) \sin^2(\beta - \alpha_1) \cos(\alpha_3) \sin(\alpha_3)$. Thus, J_1 only vanishes if the sine or cosine of $\beta - \alpha_1$ or of α_3 vanish, or if the heavier two states are degenerate. That is, J_1 vanishes in the exact alignment limit, where h_1 coincides exactly with the SM predictions, as reemphasized in Ref. [14]. What Ref. [118] brings to the table is that, as one goes slightly away from the exact alignment limit, significant *CP*-violating signals are possible in some observables, other than c_b^o.

We now turn to the flipped model, with $h_2 = h_{125}$. Our results are presented in Fig. 11. This case does allow for maximal $|c_b^o|$ couplings consistent with all current experimental data. What this means is that, in this case, one can have h_{125} coupling mostly as a scalar to the top quark, while it couples as a pure pseudoscalar to the bottom quark. Again, we notice the presence of the isolated regions (with lower radius) with $m_1 \leq 60$ GeV. For this case, the points have dominant diagrams of order 10^{-29} e.cm, unlike the

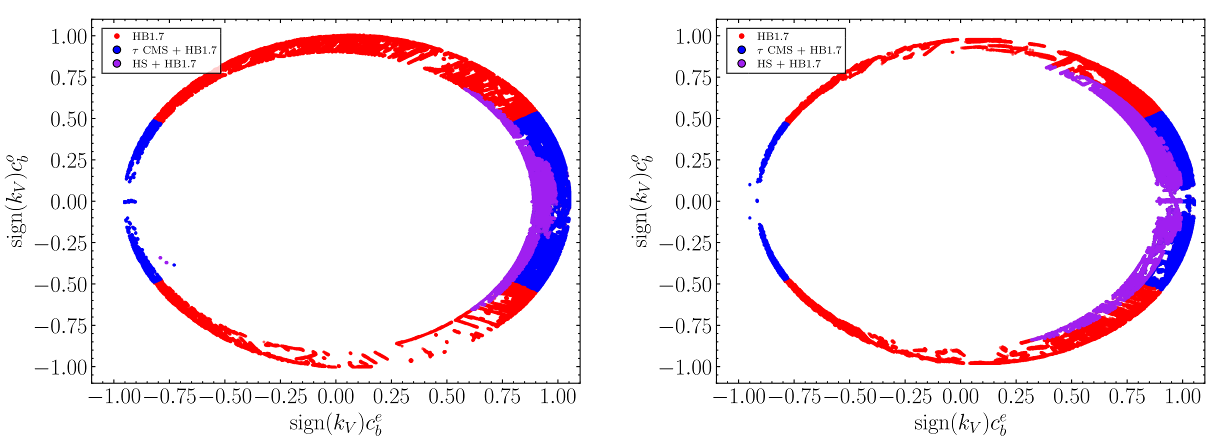

FIG. 9. Same as in Fig. 4, but for points which include the charm diagrams in the eEDM prediction.

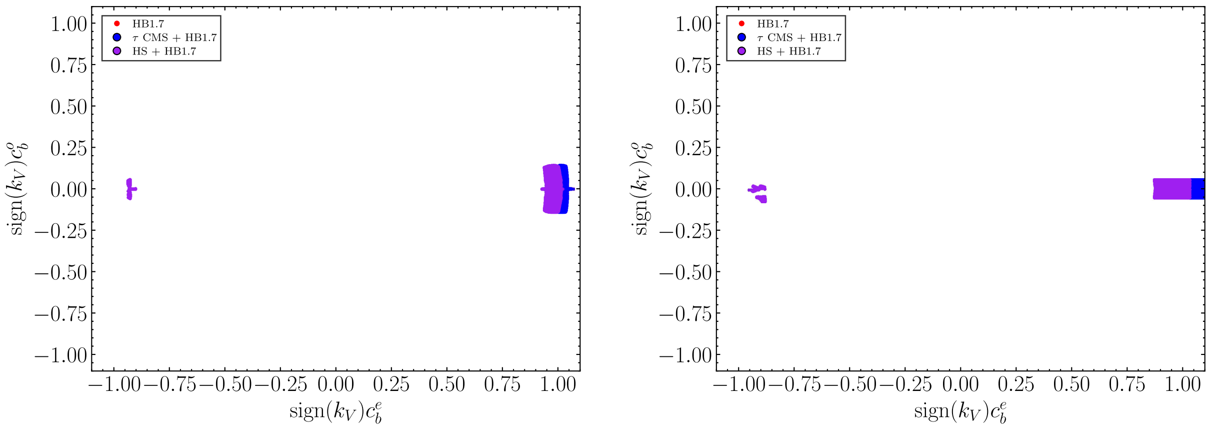

FIG. 10. Points on the plane $\mathrm{sign}(k_V)c_b^o$ vs $\mathrm{sign}(k_V)c_b^e$ obtained with strategy 2, in type II with $h_{125} = h_1$ (left) and flipped with $h_{125} = h_1$ (right). In both panels, the eEDM is calculated with the pole-masses scheme. The color code is as in Fig. 4.

order 10^{-27} e.cm individual contributions occurring in the case type II with $h_2 = h_{125}$.

VII. CONCLUSIONS

We have carried out a comprehensive exploration of the parameter space of the C2HDM using recent ML techniques designed to efficiently probe complex, high-dimensional BSM scenarios, even in the absence of preexisting training data. To this end, we employed an evolutionary strategy algorithm [69] to identify phenomenologically viable points, combined with an anomaly-detection-based novelty reward mechanism [70]. This framework enables a robust and reliable exploration of the model's parameter space and, consequently, of its potentially observable physical predictions.

We have concentrated on regions of the parameter space allowing for large components of c^o, the pseudoscalar coupling between the 125 GeV Higgs boson (h_{125}) and fermions. In particular, we were interested in the striking possibility, first pointed out in Ref. [21], that h_{125} couples to the top quark as a pure scalar, while it couples to the bottom quark as a pure pseudoscalar. Models with CP violation in the scalar sector usually must contend with large contributions to the eEDM, which is very constrained by current experiments to lie below 4.1×10^{-30} e.cm [50]. Recent articles [36,47] have pointed out the importance of kite diagrams to the theoretical issue of gauge independence of the final result, and to the practical issue of taking into account all numerically relevant contributions. Reanalyzing the C2HDM with the aid of ML, we confirmed that kite diagrams are paramount, and we further demonstrated that, at the current level of experimental precision, charm-quark Barr-Zee contributions must also be taken into account.

In the process, we investigated the sensitivity of the eEDM calculation to the renormalization prescriptions for the fermions masses, by comparing $\overline{\mathrm{MS}}$ running masses at the scale M_Z with pole masses. We found that, using the kite diagrams, the qualitative predictions for c^o made with either choice remain the same (although for different points in the model's parameter space). Moreover, the cancellations

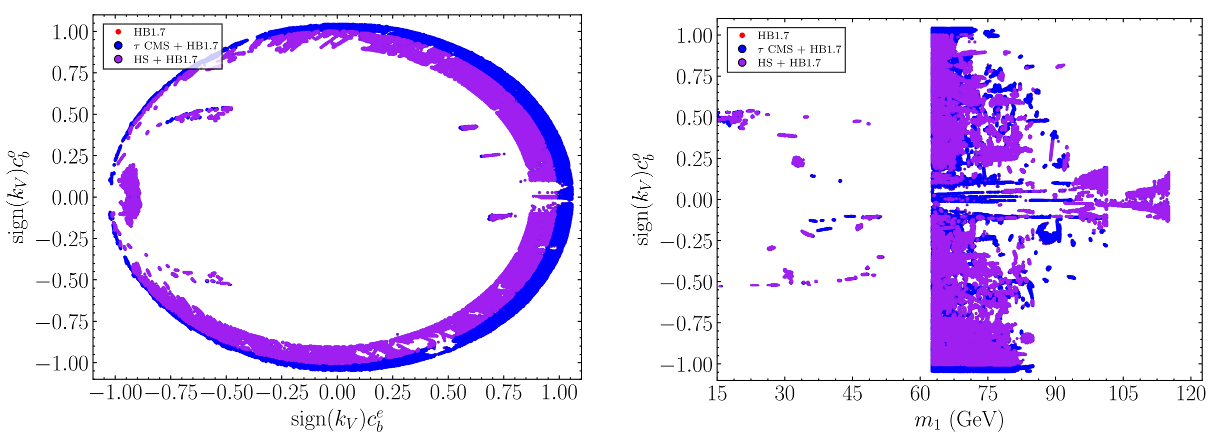

FIG. 11. Flipped C2HDM with $h_2 = h_{125}$, with the eEDM calculated with the M_Z-masses scheme, including both kite and charm contributions. The color code is as in Fig. 4. Left: plane $\mathrm{sign}(k_V)c_b^o$ vs $\mathrm{sign}(k_V)c_b^e$. Right: plane $\mathrm{sign}(k_V)c_b^o$ vs m_1.

TABLE III. Updated version of Table I after the analysis described in this paper. Underlined entries mark changes with respect to Ref. [29].

Type	I	II	LS	Flipped
$h_1 = h_{125}$	$\times$	$\times$	τ	$\times$
$h_2 = h_{125}$	$\times$	$\underline{\tau}$	τ	$\underline{\checkmark}$
$h_3 = h_{125}$	$\times$	$\times$	τ	$\times$

required to obey the current eEDM bound are still possible if the bound is improved by three orders of magnitude. As a result, such measurements will not constrain the significant c^o possibilities still available. We thus strongly encourage a continued effort to improve the direct probes for c^o at LHC. We should add that, in the C2HDM, it is not possible to accommodate large values for c^o involving the top quark. But that possibility does exist in the C3HDM, as shown in Refs. [58,76]. Hence, improved direct measurements of the *CP*-odd h_{125} to the top quark are also highly desirable.

Performing a full analyses of all model types and h_{125} assignments, we reach the conclusions shown in Table III. In type II with $h_2 = h_{125}$, $c_b^o = c_\tau^o$ is only limited by LHC's searches for *CP* violation in tau decays [56,78]; the results are shown in Fig. 9. In contrast, in the flipped model with $h_2 = h_{125}$, c_b^o can be maximal ($c_b^e = 0$); the results are shown in Fig. 11. In this second case, the wrong-sign solution ($c_b^e = -1, c_b^o = 0$) is also still viable.

In summary, we have performed a full analysis of the C2HDM utilizing ML to access the full parameter space and observable predictions, complying with the full two-loop eEDM calculation. The cases still viable call for increased experimental efforts to probe *CP*-odd h_{125} couplings to quarks directly.

ACKNOWLEDGMENTS

We thank Wolfgang Altmannshofer for discussions. D. F. thanks Joachim Brod, Gino Isidori, Kilian Möhling, Ulrich Nierste, Zachary Polonsky and Dominik Stöckinger for discussions, and the Particle Theory Group at the UZH for its hospitality and support. The work of R. B., D. F. and M. M. is supported by the Deutsche Forschungs gemeinschaft (DFG, German Research Foundation) under Grant No. 396021762-TRR 257. K. E. acknowledges financial support from the Avicenna-Studienwerk. The work of J. C. R., J. P. S., M. G. and R. S. is supported in part by the Portuguese Fundação para a Ciência e Tecnologia (FCT) through the PRR (Recovery and Resilience Plan), within the scope of the investment "RE-C06-i06—Science Plus Capacity Building," measure "RE-C06-i06.m02—Reinforcement of financing for International Partnerships in Science, Technology and Innovation of the PRR," under the projects with references No. 2024.01362.CERN and No. 2024.03328.CERN; the work is also supported by FCT under Contracts No. UIDB/00777/2020, No. UIDP/00777/2020 and No. UID/00618/2025 (https://doi.org/10.54499/UID/00618/2025). M. G. is additionally supported by FCT with a PhD Grant (Reference No. 2023.02783.BD). The FCT projects are partially funded through POCTI (FEDER), COMPETE, QREN and the EU.

DATA AVAILABILITY

There are no publicly available research data or software supporting this manuscript. Requests for further information or data should be sent to the authors.

APPENDIX A: χ^2 EXCLUSION

As explained at the end of Sec. IV A, using the public version of the HS module to impose bounds on θ_τ leads to a systematic exclusion of parameter points. In this Appendix, we provide a detailed illustration of this issue and clarify its origin. For definiteness and ease of presentation, we focus on the representative case of type II with $h_2 = h_{125}$. We stress, however, that the behavior discussed below is generic and persists in all other realizations of the C2HDM.

The systematic exclusion can be seen by considering the left panel of Fig. 12, which shows points that satisfy all constraints discussed in Sec. IV A except those relative to θ_τ. These points correspond exactly to the red points in the left panel of Fig. 2 and amount to a total of 4096 points. The exclusion is verified by realizing that, once the θ_τ constraints are applied via HS, less than 10 points survive. One might suspect that this dramatic reduction arises from limitations of the scanning procedure itself. After all, the left panel of Fig. 12 (like the corresponding panel of Fig. 2) was obtained using strategy 1, which relies on standard parameter scans. To test this hypothesis, we repeated the analysis using strategy 2. The result is shown in the right panel of Fig. 12, which displays the resulting values of $\chi^2_{\rm diff}$, which are defined in Sec. IV A and computed by HS. This plot demonstrates that the same pattern persists: only a very small number of points yields acceptably low values of $\chi^2_{\rm diff}$. Furthermore, all such points lie very close to the SM limit.

To better understand this issue, we isolate four points from Fig. 12: two from the left panel (points 1 and 3) and two from the right one (points 2 and 4). The points are described in detail in Table IV. Points 1 and 2 describe large pseudoscalar couplings, while points 3 and 4 describe small ones. Only point 3 passes HS, as it is the only one leading to a value of χ^2 close to the SM, around 150. The remaining points describe a χ^2 well above 150.

To investigate the origin of the values of χ^2, we examine the individual contributions to χ^2 of a certain point. This is done using the `chisqContributions(pred)` routine provided by HT, which allows for a comparison of all individual measurements.[4] As stated in the documentation,

[4]See the HiggsTools documentation: HiggsSignals (chisqContributions).

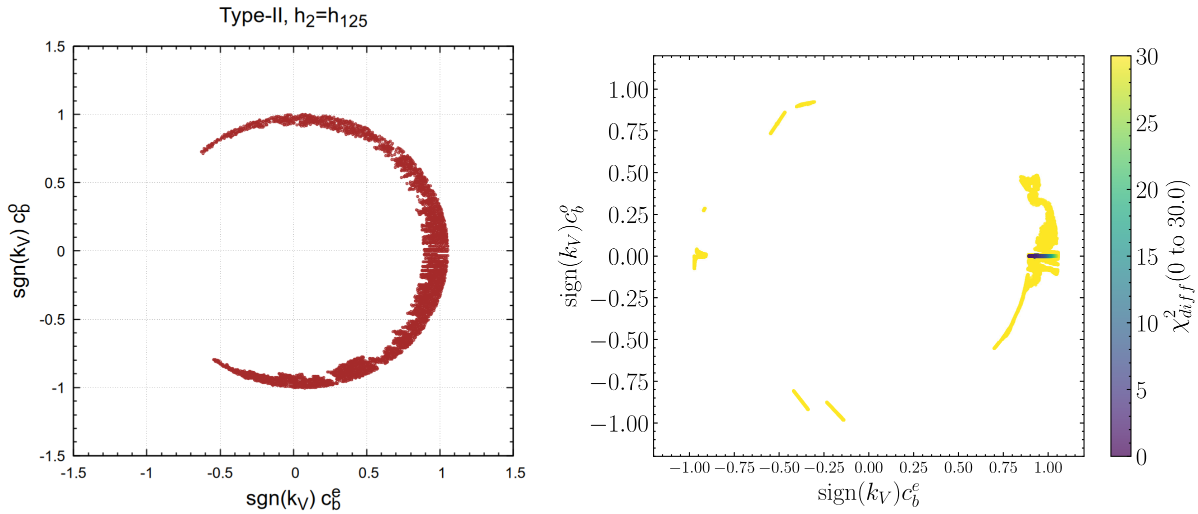

FIG. 12. Points on the plane $\mathrm{sign}(k_V)c_b^o$ vs $\mathrm{sign}(k_V)c_b^e$ in the type II C2HDM with $h_{125} = h_2$ passing all constraints except those relative to θ_τ. Left: points obtained with strategy 1. Right: points obtained with strategy 2, with 10000 points per convergence and an unseeded run. On the right, all the (yellow) points that fail HS have χ^2_{diff} of order 150.

this procedure neglects correlations and multiplicative factors, implying that the sum of the individual contributions does not coincide with the χ^2 obtained from the full combined measurement. Yet, this analysis reveals that Ref. [56] (corresponding to measurement number 13 in the HS public code) yields an anomalously large contribution to χ^2. This is confirmed by explicitly removing this measurement from the calculation, as shown in the second-to-last line of Table IV.

What exactly is the issue with Ref. [56]? This reference is implemented in HS as a multiplicity of submeasurements. Two of them are $\mu^{\tau\tau}_{ggH}$ and $\mathrm{sign}(k_V)c_\tau^o$ vs $\mathrm{sign}(k_V)c_\tau^e$,

TABLE IV. Details of four points from Fig. 12. In the public HS implementation, the SM reference value is $\chi^2_{\mathrm{SM}} = 152.54$. Removing the CMS:2021sd result [56] in its entirety reduces this value to $\chi^2_{\mathrm{SM}} = 150.2$, while removing only the $\mu_{ggH\times\tau\tau}$ submeasurement from CMS:2021sd [56] yields $\chi^2_{\mathrm{SM}} = 150.8875$.

Parameters	Point 1	Point 2	Point 3	Point 4
m_1	111.17800	117.61647	92.42560	109.20862
m_2	125.09000	125.00000	125.09000	125.00000
m_3	676.09279	676.12103	642.07726	647.28183
$m_{H^\pm}$	675.95296	653.76571	641.68967	652.61301
α_1	−0.12294140	−0.09918623	−0.20081799	−0.17832599
α_2	0.42298603	−1.00353030	0.00634782	−0.00571511
α_3	0.10171668	−0.18011110	0.00285759	−0.00211328
β	1.45177530	1.45820750	1.35522670	1.39790230
$\mathrm{Re}(m_{12}^2)$	10664.92700	37155.30600	1186.99800	1930.94000
c_t^o	−0.011073	0.01088342	−0.00006257	0.00003691
c_b^o	−0.77427177	0.85132203	−0.00130500	0.00121010
c_τ^o	−0.77427177	0.85132203	−0.00130500	0.00121010
$\mu_{ggH\times\gamma\gamma}$	0.8653	0.9369	0.9904	0.8637
$\mu_{ggH\times ZZ}$	0.9676	1.0771	1.1037	0.9572
$\mu_{ggH\times WW}$	0.9676	1.0771	1.1037	0.9572
$\mu_{ggH\times\tau\tau}$	1.0371	1.0586	0.9599	1.0177
$\mu_{ggH\times bb}$	1.0378	1.0595	0.9599	1.0177
$\mu_{ggH\times Z\gamma}$	0.9298	1.0295	1.0610	0.9214
χ^2	333.89	351.95	154.55	224.20
χ^2 w/o Ref. [56] as a whole	183.0112	185.3248	153.5897	178.0807
χ^2 w/o $\mu_{ggH\times\tau\tau} = 0.59^{+0.28}_{-0.32}$	186.6076	195.5573	154.1852	178.4548

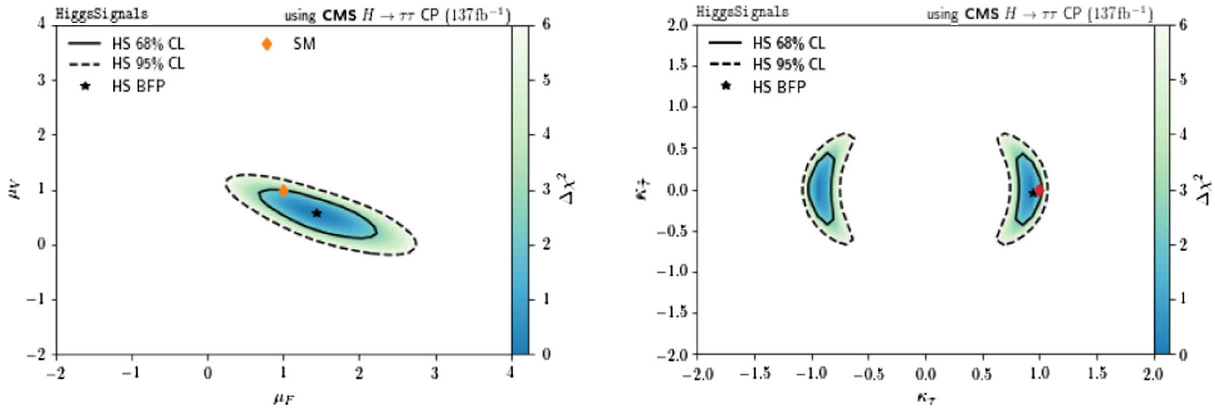

FIG. 13. Figures taken from the public HS code, describing measurement number 13, relative to Ref. [56]. Left: reported value of $\mu^{\tau\tau}_{ggH} = 0.59^{+0.28}_{-0.32}$. Right: plane $\mathrm{sign}(k_V)c^o_\tau$ vs $\mathrm{sign}(k_V)c^e_\tau$.

whose implementation in HS is shown in the left and right panels of Fig. 13, respectively. While the latter yields a physically sensible behavior—crucial for the analysis presented in this work (see the discussion in Sec. V B)—the former leads to the result that the measurement deviates from the SM at the 1σ level. Importantly, this behavior originates from the experimental result reported in Ref. [56] itself and is not an artifact of its implementation within HS. This observation can be placed in context by comparing it with the corresponding ATLAS measurements [93], which yield $\mu^{\tau\tau}_{ggF+bbH} = 0.89788^{+0.29101}_{-0.25638}$ and $\mu^{bb}_{ggF+bbH} = 0.98031^{+0.37558}_{-0.36282}$. These results are consistent with the SM expectation and do not exhibit a similar tension.

For this reason, we exclude the specific submeasurement of Ref. [56]'s $\mu^{\tau\tau}_{ggH}$ from the χ^2 evaluation in HS. In practice, this is achieved by commenting out the $\mu^{\tau\tau}_{ggH}$ entry in the corresponding HS dataset file [119]. With this single submeasurement removed, the SM reference value is updated to $\chi^2_{\mathrm{SM}} = 150.2$, compared to the original value $\chi^2_{\mathrm{SM}} = 152.54$. Reapplying HS to the parameter points shown in Fig. 12 then yields the results displayed in Fig. 14, where 400 points out of the original 4096 are now found to be compatible with the HS constraints.

APPENDIX B: EEDM FOR BENCHMARK POINTS

This Appendix contains two benchmark points in the type II which are valid under the current eEDM bound. The points are chosen such that their validity under the eEDM bound requires different renormalization prescriptions. More precisely, the first benchmark point, `BP1`, is valid under eEDM constraints only if the pole-masses scheme is chosen, while the second one, `BP2`, is valid only in the M_Z-masses scheme (recall Sec. III). Besides the eEDM constraints, these points pass all other constraints described in the main text, listed in Sec. IV A. The input

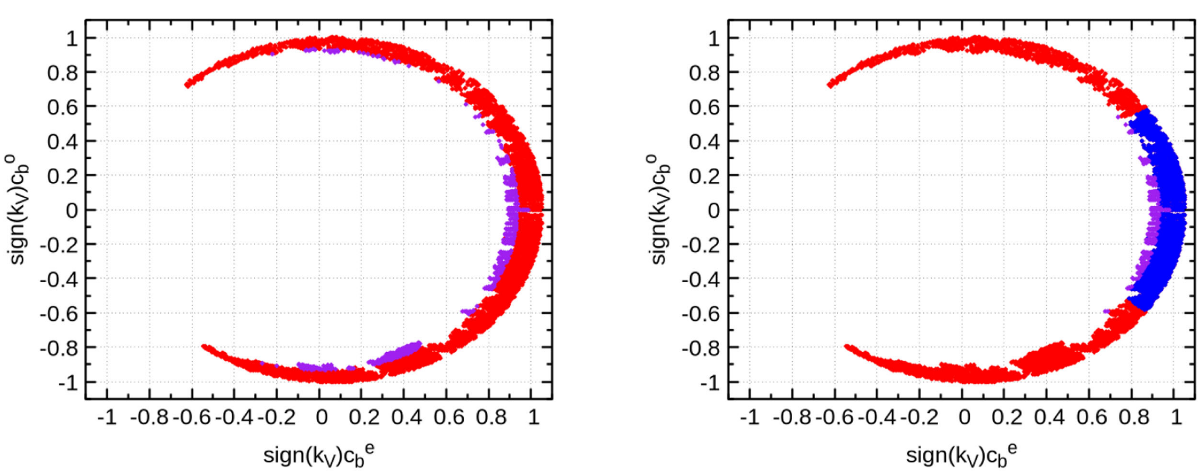

FIG. 14. Points on the plane $\mathrm{sign}(k_V)c^o_b$ vs $\mathrm{sign}(k_V)c^e_b$ in the type II C2HDM with $h_{125} = h_2$. Red points pass all constraints except those relative to θ_τ, violet points add these constraints using a modified HS: with Ref. [56] removed as a whole (left), or with only the $\mu^{\tau\tau}_{ggH}$ measurement removed (right). The right panel is identical to the left one of Fig. 2.

TABLE V. Parameter values for two benchmark points in the type II, BP1 and BP2. The table shows masses, mixing angles, and Higgs couplings to fermions.

Parameters	BP1	BP2
m_1	110.43	48.35
m_2	125.09	125.09
m_3	688.21	642.93
$m_{H^\pm}$	694.91	636.93
$\mathrm{Re}(m_{12}^2)$	2231.76	5855.64
$\tan\beta$	6.8126	1.1533
α_1	−0.1300	−0.6767
α_2	0.0846	−0.0117
α_3	0.0241	−0.0670
c^e_{tt}	1.002	1.0301
c^o_{tt}	−0.0035	0.0580
c^e_{bb}	0.8782	0.9529
c^o_{bb}	−0.1634	0.0772
$c^e_{\tau\tau}$	0.8782	0.9529
$c^o_{\tau\tau}$	−0.1634	0.0772

TABLE VI. eEDM contributions for the benchmark points BP1 and BP2, assuming the pole-masses scheme.

	BP1	BP2
d_e^f	$-1.86117130\times 10^{-27}$	$8.48660155\times 10^{-28}$
d_e^W	$2.67096242\times 10^{-27}$	$-1.17093515\times 10^{-27}$
$d_e^{H^\pm}$	$-4.16451760\times 10^{-28}$	$1.75224743\times 10^{-28}$
d_e^c	$-6.06959141\times 10^{-30}$	$4.88922925\times 10^{-30}$
d_e^{kite}	$-3.91360896\times 10^{-28}$	$1.70869973\times 10^{-28}$
d_e	$-4.09112398\times 10^{-30}$	$2.87089522\times 10^{-29}$

parameters for the two points are shown in Table V. The table also shows Yukawa couplings for both points; both

TABLE VII. eEDM contributions for the benchmark points BP1 and BP2, assuming the M_Z-masses scheme. The quantities d_e^i correspond to the diagrams described in Ref. [36] in units of e.cm.

	BP1	BP2
d_e^f	$-1.71155723\times 10^{-27}$	$8.80110332\times 10^{-28}$
d_e^W	$2.86130397\times 10^{-27}$	$-1.25437983\times 10^{-27}$
$d_e^{H^\pm}$	$-4.51280969\times 10^{-28}$	$1.90051726\times 10^{-28}$
d_e^c	$-4.54530078\times 10^{-30}$	$3.66305474\times 10^{-30}$
d_e^{kite}	$-4.19250558\times 10^{-28}$	$1.83046728\times 10^{-28}$
d_e	$2.74669914\times 10^{-28}$	$2.49201067\times 10^{-30}$

points have nonzero pseudoscalar components in the listed Yukawa couplings.

The terms that contribute to the eEDM are shown in Tables VI and VII for the pole-masses and the M_Z-masses schemes, respectively. The values were obtained with the updated version of the public code SCANNERS [108,109], that includes the kite diagrams in the eEDM calculation. The comparison between the different contributions matches the overall description given in Sec. V D. In other words, Tables VI and VII show that the cancellation among contributions needs to be very precise in order to meet the current experimental level of 4.1×10^{-30} e.cm [50]. In particular, the contributions from kite diagrams (d_e^{kite}) and fermion loops with charm quarks (d_e^c) are significant given the current experimental bound. These have already been the conclusions derived from Fig. 8, but now result from the detailed analysis of two specific benchmark points. Finally, the comparison between Tables VI and VII highlights the sensitivity of the eEDM calculation to the renormalization prescriptions for the fermions masses.

[1] T. D. Lee, A theory of spontaneous T violation, Phys. Rev. D **8**, 1226 (1973).

[2] B. Aubert *et al.* (*BABAR* Collaboration), Observation of *CP* violation in the B^0 meson system, Phys. Rev. Lett. **87**, 091801 (2001).

[3] K. Abe *et al.* (Belle Collaboration), Observation of large *CP* violation in the neutral *B* meson system, Phys. Rev. Lett. **87**, 091802 (2001).

[4] S. L. Glashow and S. Weinberg, Natural conservation laws for neutral currents, Phys. Rev. D **15**, 1958 (1977).

[5] E. A. Paschos, Diagonal neutral currents, Phys. Rev. D **15**, 1966 (1977).

[6] I. F. Ginzburg, M. Krawczyk, and P. Osland, Two Higgs doublet models with *CP* violation, in *International Workshop on Linear Colliders (LCWS 2002)* (2002), pp. 703–706, 11, arXiv:hep-ph/0211371.

[7] J. F. Gunion and H. E. Haber, The *CP* conserving two Higgs doublet model: The approach to the decoupling limit, Phys. Rev. D **67**, 075019 (2003).

[8] I. F. Ginzburg and M. Krawczyk, Symmetries of two Higgs doublet model and *CP* violation, Phys. Rev. D **72**, 115013 (2005).

[9] A. W. El Kaffas, W. Khater, O. M. Ogreid, and P. Osland, Consistency of the two Higgs doublet model and *CP* violation in top production at the LHC, Nucl. Phys. **B775**, 45 (2007).

[10] A. Arhrib, E. Christova, H. Eberl, and E. Ginina, *CP* violation in charged Higgs production and decays in the

complex two Higgs doublet model, J. High Energy Phys. 04 (2011) 089.
[11] A. Barroso, P. M. Ferreira, R. Santos, and J. P. Silva, Probing the scalar-pseudoscalar mixing in the 125 GeV Higgs particle with current data, Phys. Rev. D **86**, 015022 (2012).
[12] S. Inoue, M. J. Ramsey-Musolf, and Y. Zhang, *CP*-violating phenomenology of flavor conserving two Higgs doublet models, Phys. Rev. D **89**, 115023 (2014).
[13] D. Fontes, J. C. Romão, and J. P. Silva, $h \to Z\gamma$ in the complex two Higgs doublet model, J. High Energy Phys. 12 (2014) 043.
[14] B. Grzadkowski, O. M. Ogreid, and P. Osland, Measuring *CP* violation in Two-Higgs-Doublet models in light of the LHC Higgs data, J. High Energy Phys. 11 (2014) 084.
[15] A. W. El Kaffas, P. Osland, and O. M. Ogreid, *CP* violation, stability and unitarity of the two Higgs doublet model, Nonlin. Phenom. Complex Syst. **10**, 347 (2007).
[16] B. Grzadkowski and P. Osland, Tempered two-Higgs-doublet model, Phys. Rev. D **82**, 125026 (2010).
[17] W. Khater and P. Osland, *CP* violation in top quark production at the LHC and two Higgs doublet models, Nucl. Phys. **B661**, 209 (2003).
[18] K. Cheung, J. S. Lee, E. Senaha, and P.-Y. Tseng, Confronting higgcision with electric dipole moments, J. High Energy Phys. 06 (2014) 149.
[19] R. Grober, M. Muhlleitner, and M. Spira, Higgs pair production at NLO QCD for *CP*-violating Higgs sectors, Nucl. Phys. **B925**, 1 (2017).
[20] D. Fontes, J. C. Romão, R. Santos, and J. P. Silva, Undoubtable signs of *CP*-violation in Higgs boson decays at the LHC run 2, Phys. Rev. D **92**, 055014 (2015).
[21] D. Fontes, J. C. Romão, R. Santos, and J. P. Silva, Large pseudoscalar Yukawa couplings in the complex 2HDM, J. High Energy Phys. 06 (2015) 060.
[22] T. Abe, J. Hisano, T. Kitahara, and K. Tobioka, Gauge invariant Barr-Zee type contributions to fermionic EDMs in the two-Higgs doublet models, J. High Energy Phys. 01 (2014) 106. 04 (2016) 161(E).
[23] C.-Y. Chen, S. Dawson, and Y. Zhang, Complementarity of LHC and EDMs for exploring Higgs *CP* violation, J. High Energy Phys. 06 (2015) 056.
[24] C.-Y. Chen, H.-L. Li, and M. Ramsey-Musolf, *CP*-Violation in the two Higgs doublet model: From the LHC to EDMs, Phys. Rev. D **97**, 015020 (2018).
[25] D. Fontes, M. Mühlleitner, J. C. Romão, R. Santos, J. P. Silva, and J. Wittbrodt, The C2HDM revisited, J. High Energy Phys. 02 (2018) 073.
[26] E. J. Chun, J. Kim, and T. Mondal, Electron EDM and muon anomalous magnetic moment in two-Higgs-Doublet models, J. High Energy Phys. 12 (2019) 068.
[27] K. Cheung, A. Jueid, Y.-N. Mao, and S. Moretti, Two-Higgs-doublet model with soft *CP* violation confronting electric dipole moments and colliders, Phys. Rev. D **102**, 075029 (2020).
[28] M. Frank, E. G. Fuakye, and M. Toharia, Restricting the parameter space of type-II two-Higgs-doublet models with *CP* violation, Phys. Rev. D **106**, 035010 (2022).
[29] T. Biekötter, D. Fontes, M. Mühlleitner, J. C. Romão, R. Santos, and J. P. Silva, Impact of new experimental data on the C2HDM: The strong interdependence between LHC Higgs data and the electron EDM, J. High Energy Phys. 05 (2024) 127.
[30] M. Mühlleitner, M. O. P. Sampaio, R. Santos, and J. Wittbrodt, Phenomenological comparison of models with extended Higgs sectors, J. High Energy Phys. 08 (2017) 132.
[31] P. Basler, M. Mühlleitner, and J. Wittbrodt, The *CP*-violating 2HDM in light of a strong first order electroweak phase transition and implications for Higgs pair production, J. High Energy Phys. 03 (2018) 061.
[32] M. Aoki, K. Hashino, D. Kaneko, S. Kanemura, and M. Kubota, Probing *CP* violating Higgs sectors via the precision measurement of coupling constants, Prog. Theor. Exp. Phys. **2019**, 053B02 (2019).
[33] P. Basler, M. Mühlleitner, and J. Müller, Electroweak phase transition in non-minimal Higgs sectors, J. High Energy Phys. 05 (2020) 016.
[34] X. Wang, F. P. Huang, and X. Zhang, Gravitational wave and collider signals in complex two-Higgs doublet model with dynamical *CP*-violation at finite temperature, Phys. Rev. D **101**, 015015 (2020).
[35] R. Boto, T. V. Fernandes, H. E. Haber, J. C. Romão, and J. P. Silva, Basis-independent treatment of the complex 2HDM, Phys. Rev. D **101**, 055023 (2020).
[36] W. Altmannshofer, S. Gori, N. Hamer, and H. H. Patel, Electron EDM in the complex two-Higgs doublet model, Phys. Rev. D **102**, 115042 (2020).
[37] D. Fontes and J. C. Romão, Renormalization of the C2HDM with FeynMaster 2, J. High Energy Phys. 06 (2021) 016. 12 (2021) 005(E).
[38] P. Basler, L. Biermann, M. Mühlleitner, and J. Müller, Electroweak baryogenesis in the *CP*-violating two-Higgs doublet model, Eur. Phys. J. C **83**, 57 (2023).
[39] H. Abouabid, A. Arhrib, D. Azevedo, J. E. Falaki, P. M. Ferreira, M. Mühlleitner, and R. Santos, Benchmarking di-Higgs production in various extended Higgs sector models, J. High Energy Phys. 09 (2022) 011.
[40] D. Fontes and J. C. Romão, The one-loop impact of a dependent mass: The role of m_3 in the C2HDM, J. High Energy Phys. 03 (2022) 144.
[41] D. Azevedo, T. Biekötter, and P. M. Ferreira, 2HDM interpretations of the CMS diphoton excess at 95 GeV, J. High Energy Phys. 11 (2023) 017.
[42] D. Gonçalves, A. Kaladharan, and Y. Wu, Gravitational waves, bubble profile, and baryon asymmetry in the complex 2HDM, Phys. Rev. D **108**, 075010 (2023).
[43] S. M. Barr and A. Zee, Electric dipole moment of the electron and of the neutron, Phys. Rev. Lett. **65**, 21 (1990); **65**, 2920(E) (1990).
[44] R. G. Leigh, S. Paban, and R. M. Xu, Electric dipole moment of electron, Nucl. Phys. **B352**, 45 (1991).
[45] J. F. Gunion and R. Vega, The Electron electric dipole moment for a *CP* violating neutral Higgs sector, Phys. Lett. B **251**, 157 (1990).
[46] D. Chang, W.-Y. Keung, and T. C. Yuan, Two loop bosonic contribution to the electron electric dipole moment, Phys. Rev. D **43**, R14 (1991).

[47] W. Altmannshofer, B. Assi, J. Brod, N. Hamer, J. Julio, P. Uttayarat, and D. Volkov, Electron EDM and $\Gamma(\mu \to e\gamma)$ in the 2HDM, J. High Energy Phys. 06 (2025) 156.
[48] J. Baron *et al.* (ACME Collaboration), Order of magnitude smaller limit on the electric dipole moment of the electron, Science **343**, 269 (2014).
[49] V. Andreev *et al.* (ACME Collaboration), Improved limit on the electric dipole moment of the electron, Nature (London) **562**, 355 (2018).
[50] T. S. Roussy *et al.*, An improved bound on the electron's electric dipole moment, Science **381**, adg4084 (2023).
[51] A. C. Vutha, M. Horbatsch, and E. A. Hessels, Orientation-dependent hyperfine structure of polar molecules in a rare-gas matrix: A scheme for measuring the electron electric dipole moment, Phys. Rev. A **98**, 032513 (2018).
[52] M. Ardu, M. H. Rahat, N. Valori, and O. Vives, Electric dipole moments as indirect probes of dark sectors, J. High Energy Phys. 11 (2024) 049.
[53] M. Aiko, M. Endo, S. Kanemura, and Y. Mura, Electroweak baryogenesis in 2HDM without EDM cancellation, J. High Energy Phys. 07 (2025) 236.
[54] G. Aad *et al.* (ATLAS Collaboration), Observation of a new particle in the search for the standard model Higgs boson with the ATLAS detector at the LHC, Phys. Lett. B **716**, 1 (2012).
[55] S. Chatrchyan *et al.* (CMS Collaboration), Observation of a new boson at a mass of 125 GeV with the CMS experiment at the LHC, Phys. Lett. B **716**, 30 (2012).
[56] A. Tumasyan *et al.* (CMS Collaboration), Analysis of the CP structure of the Yukawa coupling between the Higgs boson and τ leptons in proton-proton collisions at $\sqrt{s} = 13$ TeV, J. High Energy Phys. 06 (2022) 012.
[57] R. Boto, L. Lourenco, J. C. Romão, and J. P. Silva, Large pseudoscalar Yukawa couplings in the complex 3HDM, J. High Energy Phys. 11 (2024) 106.
[58] F. A. de Souza, R. Boto, M. Crispim Romão, P. N. Figueiredo, J. C. Romão, and J. P. Silva, Unearthing large pseudoscalar Yukawa couplings with machine learning, J. High Energy Phys. 07 (2025) 268.
[59] M. Feickert and B. Nachman, A living review of machine learning for particle physics.
[60] P. Shanahan *et al.*, Snowmass 2021 computational frontier CompF03 topical group report: Machine learning, arXiv:2209.07559.
[61] T. Plehn, A. Butter, B. Dillon, T. Heimel, C. Krause, and R. Winterhalder, Modern machine learning for LHC physicists, arXiv:2211.01421.
[62] S. Caron, T. Heskes, S. Otten, and B. Stienen, Constraining the parameters of high-dimensional models with active learning, Eur. Phys. J. C **79**, 944 (2019).
[63] J. Hollingsworth, M. Ratz, P. Tanedo, and D. Whiteson, Efficient sampling of constrained high-dimensional theoretical spaces with machine learning, Eur. Phys. J. C **81**, 1138 (2021).
[64] M. D. Goodsell and A. Joury, Active learning BSM parameter spaces, Eur. Phys. J. C **83**, 268 (2023).
[65] M. A. Diaz, G. Cerro, S. Dasmahapatra, and S. Moretti, Bayesian active search on parameter space: A 95 GeV spin-0 resonance in the $(B-L)$SSM, SciPost Phys. Core **8**, 068 (2025).
[66] S. AbdusSalam, S. Abel, and M. C. Romão, Symbolic regression for beyond the standard model physics, Phys. Rev. D **111**, 015022 (2025).
[67] N. Batra, B. Coleppa, A. Khanna, S. K. Rai, and A. Sarkar, Constraining the 3HDM parameter space, Phys. Rev. D **112**, 015011 (2025).
[68] A. Hammad, R. Ramos, A. Chakraborty, P. Ko, and S. Moretti, Explaining data anomalies over the NMSSM parameter space with deep learning techniques, J. High Energy Phys. 02 (2026) 077.
[69] F. Abreu de Souza, M. Crispim Romão, N. F. Castro, M. Nikjoo, and W. Porod, Exploring parameter spaces with artificial intelligence and machine learning black-box optimization algorithms, Phys. Rev. D **107**, 035004 (2023).
[70] J. Crispim Romão and M. Crispim Romão, Combining evolutionary strategies and novelty detection to go beyond the alignment limit of the Z3 3HDM, Phys. Rev. D **109**, 095040 (2024).
[71] H. Georgi and D. V. Nanopoulos, Suppression of flavor changing effects from neutral spinless meson exchange in gauge theories, Phys. Lett. B **82**, 95 (1979).
[72] J. F. Donoghue and L. F. Li, Properties of charged Higgs bosons, Phys. Rev. D **19**, 945 (1979).
[73] L. Lavoura and J. P. Silva, Fundamental CP violating quantities in a $\mathrm{SU}(2) \times \mathrm{U}(1)$ model with many Higgs doublets, Phys. Rev. D **50**, 4619 (1994).
[74] F. J. Botella and J. P. Silva, Jarlskog—like invariants for theories with scalars and fermions, Phys. Rev. D **51**, 3870 (1995).
[75] F. A. de Souza, N. F. Castro, M. Crispim Romão, and W. Porod, Exploring scotogenic parameter spaces and mapping uncharted dark matter phenomenology with multi-objective search algorithms, J. High Energy Phys. 10 (2025) 116.
[76] R. Boto, J. A. C. Matos, J. C. Romão, and J. P. Silva, Surveying the complex three Higgs doublet model with machine learning, J. High Energy Phys. 03 (2026) 182.
[77] G. Aad *et al.* (ATLAS Collaboration), CP Properties of Higgs boson interactions with top quarks in the $t\bar{t}H$ and tH processes using $H \to \gamma\gamma$ with the ATLAS detector, Phys. Rev. Lett. **125**, 061802 (2020).
[78] G. Aad *et al.* (ATLAS Collaboration), Measurement of the CP properties of Higgs boson interactions with τ-leptons with the ATLAS detector, Eur. Phys. J. C **83**, 563 (2023).
[79] N. Yamanaka, Analysis of the electric dipole moment in the R-parity violating supersymmetric standard model, Ph.D. thesis, Osaka U., 2013, 10.1007/978-4-431-54544-6.
[80] S. F. King, M. Muhlleitner, R. Nevzorov, and K. Walz, Exploring the CP-violating NMSSM: EDM constraints and phenomenology, Nucl. Phys. **B901**, 526 (2015).
[81] H. Bahl, E. Fuchs, S. Heinemeyer, J. Katzy, M. Menen, K. Peters, M. Saimpert, and G. Weiglein, Constraining the $\mathcal{CP}$ structure of Higgs-fermion couplings with a global LHC fit, the electron EDM and baryogenesis, Eur. Phys. J. C **82**, 604 (2022).
[82] K. G. Klimenko, On necessary and sufficient conditions for some Higgs potentials to be bounded from below, Theor. Math. Phys. **62**, 58 (1985).

[83] P. M. Ferreira and D. R. T. Jones, Bounds on scalar masses in two Higgs doublet models, J. High Energy Phys. 08 (2009) 069.
[84] I. P. Ivanov, Minkowski space structure of the Higgs potential in 2HDM, Phys. Rev. D **75**, 035001 (2007). **76**, 039902(E) (2007).
[85] I. P. Ivanov and J. P. Silva, Tree-level metastability bounds for the most general two Higgs doublet model, Phys. Rev. D **92**, 055017 (2015).
[86] S. Kanemura, T. Kubota, and E. Takasugi, Lee-Quigg-Thacker bounds for Higgs boson masses in a two doublet model, Phys. Lett. B **313**, 155 (1993).
[87] A. G. Akeroyd, A. Arhrib, and E.-M. Naimi, Note on tree level unitarity in the general two Higgs doublet model, Phys. Lett. B **490**, 119 (2000).
[88] I. F. Ginzburg and I. P. Ivanov, Tree level unitarity constraints in the 2HDM with *CP* violation, arXiv:hep-ph/0312374.
[89] W. Grimus, L. Lavoura, O. M. Ogreid, and P. Osland, A precision constraint on multi-Higgs-doublet models, J. Phys. G **35**, 075001 (2008).
[90] W. Grimus, L. Lavoura, O. M. Ogreid, and P. Osland, The oblique parameters in multi-Higgs-doublet models, Nucl. Phys. **B801**, 81 (2008).
[91] M. Baak, J. Cúth, J. Haller, A. Hoecker, R. Kogler, K. Mönig, M. Schott, and J. Stelzer (Gfitter Group Collaboration), The global electroweak fit at NNLO and prospects for the LHC and ILC, Eur. Phys. J. C **74**, 3046 (2014).
[92] G. Aad *et al.* (ATLAS Collaboration), Combined measurements of Higgs boson production and decay using up to 80 fb^{-1} of proton-proton collision data at $\sqrt{s} = 13$ TeV collected with the ATLAS experiment, Phys. Rev. D **101**, 012002 (2020).
[93] G. Aad *et al.* (ATLAS Collaboration), A detailed map of Higgs boson interactions by the ATLAS experiment ten years after the discovery, Nature (London) **607**, 52 (2022); **612**, E24 (2022).
[94] A. Tumasyan *et al.* (CMS Collaboration), A portrait of the Higgs boson by the CMS experiment ten years after the discovery., Nature (London) **607**, 60 (2022); **623**, E4 (2023).
[95] H. Bahl, T. Biekötter, S. Heinemeyer, C. Li, S. Paasch, G. Weiglein, and J. Wittbrodt, HiggsTools: BSM scalar phenomenology with new versions of HiggsBounds and HiggsSignals, Comput. Phys. Commun. **291**, 108803 (2023).
[96] F. M. Borzumati and C. Greub, 2HDMs predictions for anti-B—> X(s) gamma in NLO QCD, Phys. Rev. D **58**, 074004 (1998).
[97] Y. S. Amhis *et al.* (HFLAV Collaboration), Averages of b-hadron, c-hadron, and τ-lepton properties as of 2018, Eur. Phys. J. C **81**, 226 (2021).
[98] O. Deschamps, S. Monteil, V. Niess, S. Descotes-Genon, S. T'Jampens, and V. Tisserand, The two Higgs doublet of type II facing flavour physics data, Phys. Rev. D **82**, 073012 (2010).
[99] F. Mahmoudi and O. Stal, Flavor constraints on the two-Higgs-doublet model with general Yukawa couplings, Phys. Rev. D **81**, 035016 (2010).
[100] T. Hermann, M. Misiak, and M. Steinhauser, $\bar{B} \to X_s\gamma$ in the two Higgs doublet model up to next-to-next-to-leading order in QCD, J. High Energy Phys. 11 (2012) 036.
[101] M. Misiak *et al.*, Updated NNLO QCD predictions for the weak radiative B-meson decays, Phys. Rev. Lett. **114**, 221801 (2015).
[102] M. Misiak and M. Steinhauser, Weak radiative decays of the B meson and bounds on $M_{H^\pm}$ in the two-Higgs-doublet model, Eur. Phys. J. C **77**, 201 (2017).
[103] J. Haller, A. Hoecker, R. Kogler, K. Mönig, T. Peiffer, and J. Stelzer, Update of the global electroweak fit and constraints on two-Higgs-doublet models, Eur. Phys. J. C **78**, 675 (2018).
[104] H. E. Haber and D. O'Neil, Basis-independent methods for the two-Higgs-doublet model III: The *CP*-conserving limit, custodial symmetry, and the oblique parameters S, T, U, Phys. Rev. D **83**, 055017 (2011).
[105] N. Hansen and A. Ostermeier, Completely derandomized self-adaptation in evolution strategies, Evol. Comput. **9**, 159 (2001).
[106] N. Hansen, The CMA evolution strategy: A tutorial, arXiv:1604.00772.
[107] M. Goldstein and A. Dengel, Histogram-based outlier score (HBOS): A fast unsupervised anomaly detection algorithm, in *KI-2012: Poster and Demo Track*, edited by S. Wölfl (German Research Center for Artificial Intelligence (DFKI), Saarbrücken, Germany, 2012).
[108] R. Coimbra, M. O. P. Sampaio, and R. Santos, Scanners: Constraining the phase diagram of a complex scalar singlet at the lhc, Eur. Phys. J. C **73**, 2428 (2013).
[109] M. Mühlleitner, M. O. P. Sampaio, R. Santos, and J. Wittbrodt, ScannerS: Parameter scans in extended scalar sectors, Eur. Phys. J. C **82**, 198 (2022).
[110] A. M. Sirunyan *et al.* (CMS Collaboration), Search for additional neutral MSSM Higgs bosons in the $\tau\tau$ final state in proton-proton collisions at $\sqrt{s} = 13$ TeV, J. High Energy Phys. 09 (2018) 007.
[111] A. Tumasyan *et al.* (CMS Collaboration), Searches for additional Higgs bosons and for vector leptoquarks in $\tau\tau$ final states in proton-proton collisions at $\sqrt{s} = 13$ TeV, J. High Energy Phys. 07 (2023) 073.
[112] G. Aad *et al.* (ATLAS Collaboration), Search for heavy resonances decaying into a Z or W boson and a Higgs boson in final states with leptons and b-jets in 139 fb^{-1} of pp collisions at $\sqrt{s} = 13$ TeV with the ATLAS detector, J. High Energy Phys. 06 (2023) 016.
[113] C. Peset, A. Pineda, and J. Segovia, The charm/bottom quark mass from heavy quarkonium at N^3LO, J. High Energy Phys. 09 (2018) 167.
[114] A. Denner, S. Dittmaier, M. Grazzini, R. V. Harlander, R. S. Thorne, M. Spira *et al.*, Standard model input parameters for Higgs physics.
[115] M. Aaboud *et al.* (ATLAS Collaboration), Combination of searches for heavy resonances decaying into bosonic and leptonic final states using 36 fb^{-1} of proton-proton collision data at $\sqrt{s} = 13$ TeV with the ATLAS detector, Phys. Rev. D **98**, 052008 (2018).
[116] G. Aad *et al.* (ATLAS Collaboration), Search for heavy resonances decaying into a pair of Z bosons in the $\ell^+\ell^-\ell\prime^+\ell\prime^-$ and $\ell^+\ell^-\nu\bar{\nu}$ final states using 139 fb^{-1} of

proton-proton collisions at $\sqrt{s} = 13$ TeV with the ATLAS detector, Eur. Phys. J. C **81**, 332 (2021).

[117] G. Aad *et al.* (ATLAS Collaboration), Search for resonant and non-resonant Higgs boson pair production in the $b\bar{b}\tau^+\tau^-$ decay channel using 13 TeV pp collision data from the ATLAS detector, J. High Energy Phys. 07 (2023) 040.

[118] S. Lee, A. Hammad, D. Kim, and J. Song, Intrinsic properties of large CP violation in the complex two-Higgs-doublet model, Phys. Rev. D **113**, 115034 (2026).

[119] https://gitlab.com/higgsbounds/hsdataset/-/blob/main/h125/tautau_CP_LHC13_CMS_137.json?ref_Type=heads.